

AC Loss Modeling in HTS Machines for Turboelectric Propulsion in Aircraft

A Thesis

Presented to

the Faculty of the Department of Mechanical Engineering

University of Houston

In Partial Fulfillment

of the Requirements for the Degree

Master of Science

in Mechanical Engineering

By

Virginia Elizabeth Phifer

August 2017

AC Loss Modeling in HTS Machines for Turboelectric Propulsion in Aircraft

Virginia Elizabeth Phifer

Approved:

Committee Chair
Dr. Phillip Masson, Assistant Professor
of Mechanical Engineering

Committee Members:

Dr. Pradeep Sharma, M.D. Anderson
Chair Professor & Department Chair of
Mechanical Engineering

Dr. Di Yang, Assistant Professor of
Mechanical Engineering

Dr. Suresh K. Khator, Associate Dean,
Cullen College of Engineering

Dr. Pradeep Sharma, M.D. Anderson
Chair Professor & Department Chair of
Mechanical Engineering

ACKNOWLEDGEMENTS

I would like to thank Dr. Philippe Masson for his guidance throughout my research, to Dr. Renuka Rajput-Ghoshal for introducing me to superconductivity, and to my parents for their unfailing love and support.

AC Loss Modeling in HTS Machines for Turboelectric Propulsion in Aircraft

An Abstract

of a

Thesis

Presented to

the Faculty of the Department of Mechanical Engineering

University of Houston

In Partial Fulfillment

of the Requirements for the Degree

Master of Science

in Mechanical Engineering

By

Virginia Elizabeth Phifer

August 2017

ABSTRACT

As environmental concern increases, the aircraft industry is looking toward distributed propulsion to improve efficiency and reduce emissions. Superconducting turbo-electric motors and generators replace traditional high-bypass ratio turbine engines. However, superconductors are susceptible to large AC losses when subjected to variable magnetic fields. Thus accurate loss calculations are crucial in determining the optimum weight of a superconducting machine. This paper expands upon 3-D models, comprising a low fidelity zeroth order and high fidelity electromagnetic, thermal, and structural models, developed to size fully superconducting machines. Improvements focused on the electromagnetic analysis in the zeroth order model by updating solutions to the magnetic field and AC losses, resulting in more accurate solutions. Many superconducting machines use copper stator windings, eliminating large AC losses, but copper is resistive, requiring more mass to produce the same power as a superconductor. The mass of fully and partially superconducting machines was compared to determine which system is better suited for turbo-electric propulsion.

| | |
|---|-----|
| TABLE OF CONTENTS | |
| ACKNOWLEDGEMENTS | iv |
| ABSTRACT | vi |
| TABLE OF CONTENTS | vii |
| LIST OF FIGURES | ix |
| LIST OF TABLES | xi |
| NOMENCLATURE | xii |
| 1. INTRODUCTION | 1 |
| 1.1 Air Traffic Forecast | 1 |
| 1.2 Future Aircraft Designs | 4 |
| 1.3 Superconducting Machines | 5 |
| 1.4 Problem Statement | 6 |
| 1.5 Thesis Structure | 7 |
| 2. BACKGROUND | 8 |
| 2.1 Current Aircraft Design | 8 |
| 2.2 Turboelectric Propulsion | 9 |
| 2.3 Superconductivity | 12 |
| 2.4 AC Losses | 19 |
| 2.4.1 Hysteresis Losses and the Critical State (Bean) Model | 20 |
| 2.4.2 Coupling Losses | 24 |
| 2.4.3 Eddy Current Losses | 24 |
| 3. THE MODEL | 26 |
| 3.1 Overview of Electromagnetic Model in AMBER | 27 |
| 3.2 Structure of SIZING | 28 |
| 3.3.1 Stator Volume Calculation | 35 |
| 3.3.2 Magnetic Field Corrections | 38 |
| 3.3.3 AC Loss Corrections | 40 |
| 3.3.4 Copper Stator | 45 |
| 3.3.5 SIZING as a Stand-Alone Program | 46 |
| 3.4 AMBER Updates | 46 |
| 4. RESULTS | 47 |
| 4.1 Magnetic Field | 47 |
| 4.2 AC Losses | 48 |

| | |
|---------------------------------------|----|
| 4.2.1 Hysteresis Losses | 52 |
| 4.2.2 Eddy Current Losses | 52 |
| 4.2.3 Coupling Losses | 53 |
| 4.3 Mass | 54 |
| 4.4 Copper v. MgB ₂ Stator | 56 |
| 5. CONCLUSIONS | 59 |
| REFERENCES | 61 |

LIST OF FIGURES

| | |
|--|----|
| Figure 1.1: FAA forecast of U.S. commercial air carriers domestic market through 2036 | 2 |
| Figure 1.2: FAA forecast of increase in passengers on U.S. domestic (blue) and international (orange) flights through 2036 | 2 |
| Figure 1.3: Breakdown of U.S. greenhouse gas emissions | 3 |
| Figure 1.4: Projected environmental impact from CO ₂ emissions with (a) moderate advances in airplane technology and (b) significant advances | 4 |
| Figure 2.1: Reduction to aircraft noise level over the years | 8 |
| Figure 2.2: Reduction in fuel burn throughout the years | 9 |
| Figure 2.3: HWB distributed propulsion conceptual design | 10 |
| Figure 2.4: Distributed turbo-electric propulsion conceptual design | 11 |
| Figure 2.5: Qualitative plot of resistivity against temperature | 13 |
| Figure 2.6: Critical surface for the superconductor niobium-titanium (NbTi) | 14 |
| Figure 2.7: Meissner Effect in Type I superconductors | 15 |
| Figure 2.8: Magnetization of Type II superconductors, below B_{c1} they are perfectly diamagnetic, between B_{c1} and B_{c2} some flux is allowed to penetrate the conductor, above B_{c2} superconductivity breaks down | 17 |
| Figure 2.9: Critical current versus magnetic field for various superconducting materials | 18 |
| Figure 2.10: T_c of various superconducting materials | 19 |
| Figure 2.11: Superconducting filamentary composite wire | 20 |
| Figure 2.12: Screening Currents/critical state model | 21 |
| Figure 2.13: Qualitative hysteresis loop for a superconductor | 22 |
| Figure 2.14: Coupling currents flows along filament then drops vertically through the composite to the opposite filament | 25 |
| Figure 3.1: Basic structure of 3-d sizing program | 26 |
| Figure 3.2: 3-D machine geometry | 27 |
| Figure 3.3: Basic machine geometry and important parameters calculated in SIZING | 28 |
| Figure 3.4: A 2-D cross section of the geometry, determined in SIZING, depicts a few of the structural parameters. MLI stands for multi-layer insulation and is used to reduce heat loss due to radiation | 29 |
| Figure 3.5: Qualitative plot of operation point compared to the maximum, or critical point | 30 |
| Figure 3.6: Difference in AC losses calculated in SIZING (blue) and AMBER (orange), with the respective percent error labeled for each case | 32 |
| Figure 3.7: Difference in hysteresis losses calculated in SIZING (blue) and AMBER (orange), with the respective percent error labeled for each case | 33 |
| Figure 3.8: Difference in eddy current losses calculated in SIZING (blue) and AMBER (orange), with the respective percent error labeled for each case | 33 |

| | |
|--|----|
| Figure 3.9: Difference in coupling losses calculated in SIZING (blue) and AMBER (orange), with the respective percent error labeled for each case | 34 |
| Figure 3.10: Stator showing 3 phases of saddle coils denoting the coil ends and straight sections of the coils | 35 |
| Figure 3.11: Parameters used in calculation of saddle coil volume | 36 |
| Figure 3.12: Field ellipticity plotted against machine torque | 43 |
| Figure 3.13: Field ellipticity plotted against the rotor-stator air gap | 43 |
| Figure 3.14: Field ellipticity plotted against machine torque for the updated model | 44 |
| Figure 3.15: Effect of ellipticity on hysteresis losses | 45 |
| Figure 4.1: Comparison of the percent error for the magnetic field between SIZING and AMBER in the original (blue) and updated (orange) program | 48 |
| Figure 4.2: Comparison of the percent error for the total losses between SIZING and AMBER in the original (blue) and updated (orange) program | 49 |
| Figure 4.3: Comparison of total AC losses between SIZING (blue) and AMBER (orange) in the updated model | 50 |
| Figure 4.4: AC Loss distribution from the original model for SIZING (blue) and AMBER (orange). Only cases for $P = 8000 \text{ kW}$ are shown. | 51 |
| Figure 4.5: AC Loss distribution from the updated model for SIZING (blue) and AMBER (orange). Only cases for $P = 8000 \text{ kW}$ are shown. | 51 |
| Figure 4.7: Comparison of the percent error for the hysteresis losses between SIZING and AMBER in the original (blue) and updated (orange) program | 52 |
| Figure 4.8: Comparison of the percent error for the eddy current losses between SIZING and AMBER in the original (blue) and updated (orange) program | 53 |
| Figure 4.9: Comparison of the percent error for the coupling losses between SIZING and AMBER in the original (blue) and updated (orange) program | 54 |
| Figure 4.10: Comparison of the percent error for the mass between SIZING and AMBER in the original (blue) and updated (orange) program | 55 |
| Figure 4.11: Difference in mass between SIZING (blue) and AMBER (orange) for the updated program | 55 |
| Figure 4.12: Difference in mass between Sizing (blue) and Amber (orange) for the original program | 56 |
| Figure 4.13: Active machine mass for a superconducting machine with a copper stator (orange) with $J = 5 \text{ A/mm}^2$ and an MgB2 stator (blue) | 57 |
| Figure 4.14: Active machine mass for a superconducting machine with a copper stator (orange) with $J = 7 \text{ A/mm}^2$ and an MgB2 stator (blue) | 58 |

LIST OF TABLES

| | |
|--|----|
| Table 1.1 NASA's Goals for Aircraft Design (STOL) | 5 |
| Table 2.1: Critical Temperature and Field of Type I superconductors | 16 |
| Table 2.2: Critical Temperature, Field, and Current Density in Type II Superconductors | 17 |
| Table 3.1: Simulations with Significant Ellipticity Differences | 45 |
| Table 4.1: Simulation power and speed specifications | 47 |

NOMENCLATURE

| Symbol | Description | Unit |
|-----------------|---|----------|
| A | Magnetic vector potential | |
| b_0 | Magnitude of magnetic flux density | T |
| b^* | Reduced magnetic flux density | |
| B | Magnetic flux density | T |
| B_0 | No load magnetic field | T |
| B_a | Applied magnetic field | T |
| B_c | Critical magnetic field | T |
| B_{c1} | Lower critical magnetic field | T |
| B_{c2} | Upper critical magnetic field | T |
| B_m | Peak magnetic field in conductor | T |
| B_{max} | Maximum field in wire | T |
| B_{min} | Minimum field in wire | T |
| B_{Rt_r} | Radial component of rotor magnetic field | T |
| B_{Rt_θ} | θ -component of rotor magnetic field | T |
| B_{St_r} | Radial component of stator magnetic field | T |
| B_{St_θ} | θ -component of stator magnetic field | T |
| $B_{St_{max}}$ | Maximum magnetic field in stator | T |
| d_1 | Outer diameter of curved section of saddle coil | m |
| d_2 | Inner diameter of curved section of saddle coil | m |
| dB | Magnetic field difference | T |
| d_{cond} | Conductor/wire diameter | m |
| d_{fil} | Filament diameter | m |
| D_{St} | Density of superconductor in the stator | kg/m^3 |
| E | Electric Field | V/m |
| E_c | Electric field criterion | V/m |
| e_s | Stator thickness | m |
| e_{St} | Thickness of one stator phase | m |
| f | Frequency | Hz |
| f^* | Reduced frequency | |
| H | Magnetic field strength | A/m |
| i | Current | A |
| $istst$ | Spacing between stator phases | m |
| J | Current density | A/mm^2 |
| J_c | Critical current density | A/mm^2 |
| J_s | Operating current | A/mm^2 |
| k | Field ellipticity | |
| k_w | Winding factor | |
| K | Current sheet approximation | A/m |
| K_r | Rotor electrical loading | A/m |
| K_s | Stator electrical loading | A/m |
| L_a | Machine active length | m |
| M | Magnetization | A/m |

| | | |
|----------------|--|---------------------|
| M_{Cu-SC} | Ratio of copper matrix to superconducting filament | |
| n | n-value | |
| p | Pairs of poles | |
| P | Power | W |
| P_g | Generated power | W |
| q^* | Reduced losses | |
| Q | Losses | W |
| Q_C | Coupling Losses | W |
| Q_E | Eddy current losses | W |
| Q_H | Hysteresis Losses | W |
| Q_{Tot} | Total AC Losses | W |
| r | Radius | m |
| r_0 | Average stator radius | m |
| r_1 | Rotor inner radius | m |
| r_2 | Rotor outer radius | m |
| r_e | Back iron outer radius | m |
| r_s | Back iron inner radius | m |
| r_f | Average field (rotor) winding radius | m |
| Ri_{St-ph} | Inner radius of stator phases | m |
| SF | Shape factor | |
| St_{fill} | Filling factor | |
| T | Temperature | K |
| T_{ph} | Turns per phase | |
| T_c | Critical temperature | K |
| TP | Twist Pitch | m |
| T_{op} | Operating temperature | K |
| V_{wire} | Volume of wire | m^3 |
| V_{St} | Volume of stator | m^3 |
| W_{St} | Stator weight | kg |
| γ | Elliptical loss ratio | |
| θ_{saf} | Angle between two saddle coils in stator | rad |
| λ | Penetration depth | m |
| μ_0 | Vacuum permittivity | Tm/A |
| ρ | Electrical resistivity | Ωm |
| σ | Electrical conductivity | $\Omega^{-1}m^{-1}$ |
| τ | Torque | Nm |
| φ | Phase angle between rotating and alternating magnetic fields | rad |
| Φ | Magnetic flux | Vs |
| ω | Angular frequency | rad/s |

1. INTRODUCTION

1.1 Air Traffic Forecast

The world today is more interconnected than ever before. Advances in technology unite people, ideas, culture, and products around the world. The airplane makes domestic, as well as, international travel easy, fast, and convenient. As the world becomes increasingly related, experts predict that air traffic will increase [1].

The Federal Aviation Administration (FAA) predicts that air system traffic, reported in Revenue Passenger Miles (RPMs), will increase by 2.6% per year for the next 20 years, with a growth rate of 2.1% and 3.5% per year in U.S domestic and international flights, respectively. Air system capacity, measured as Available Seat Miles (ASMs) is expected to increase correspondingly with RPMs. These two parameters are used to determine the load factor as, $Load\ Factor = \frac{RPMs}{ASMs} * 100$, which measures the system's use against its capacity.

Figs. 1.1 and 1.2 highlights the FAA's air traffic forecasts through 2036. As the number of passengers increase, capacity must increase to meet demands. The FAA predicts that by 2036 there will only be a few 50-seat regional aircraft left in operation, being replaced with larger 70 to 90-seat regional aircraft. Without new innovative designs, as system use and aircraft size increase, noise levels and takeoff and landing distances will increase. In order to continue using current airport infrastructure, aircraft manufactures need to reduce noise, take off, and landing distances, since many airports, located in urban environments, lack the space to expand [1].

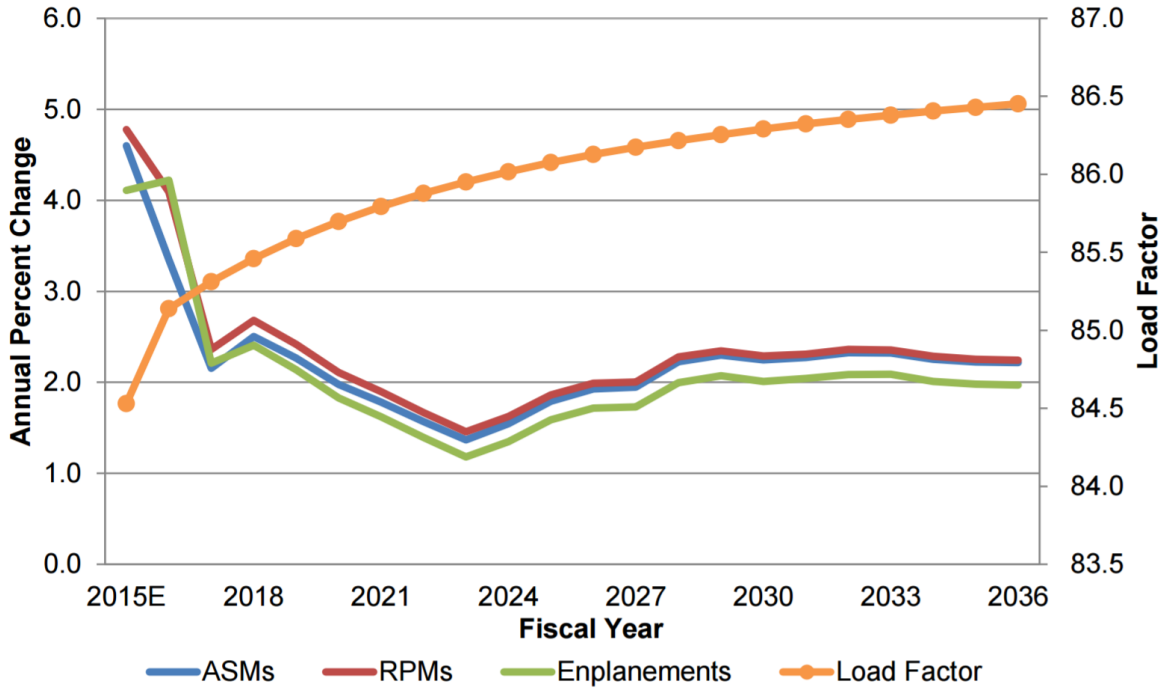


Figure 1.1: FAA forecast of U.S. commercial air carriers domestic market through 2036[1]

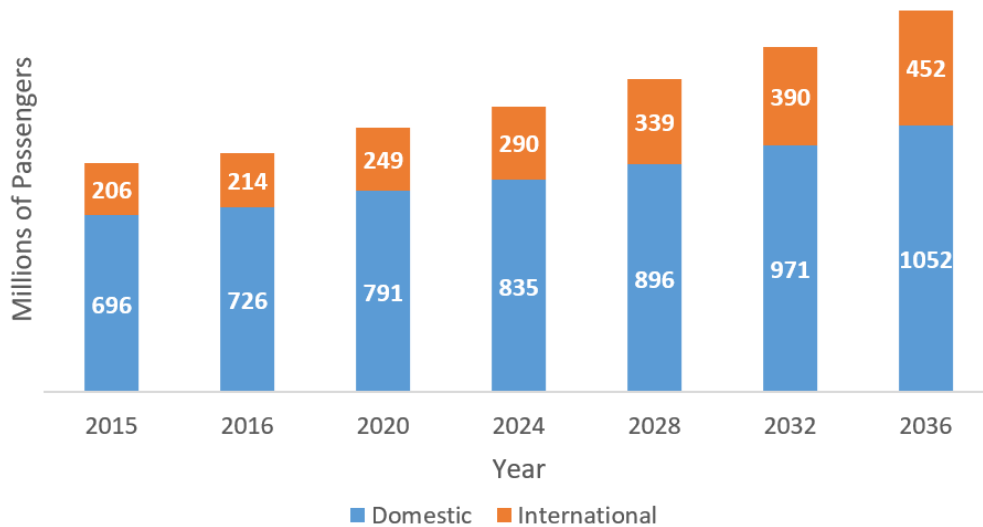


Figure 1.2: FAA forecast of increase in passengers on U.S. domestic (blue) and international (orange) flights through 2036[1]

In addition to the increasing strains on airlines is an ever-increasing concern for the environment. According to models developed by Mora et al. in [2], average temperatures in tropical areas are expected to move above historical variability as early as the year 2020,

with temperatures near the poles increasing as much as 15°C by 2080. The EPA reports that the transportation sector constitutes 27% of all greenhouse gas emissions, shown in Fig. 1.3, and as more airplanes take to the skies, unless designs change, it is inevitable that emissions will increase [3].

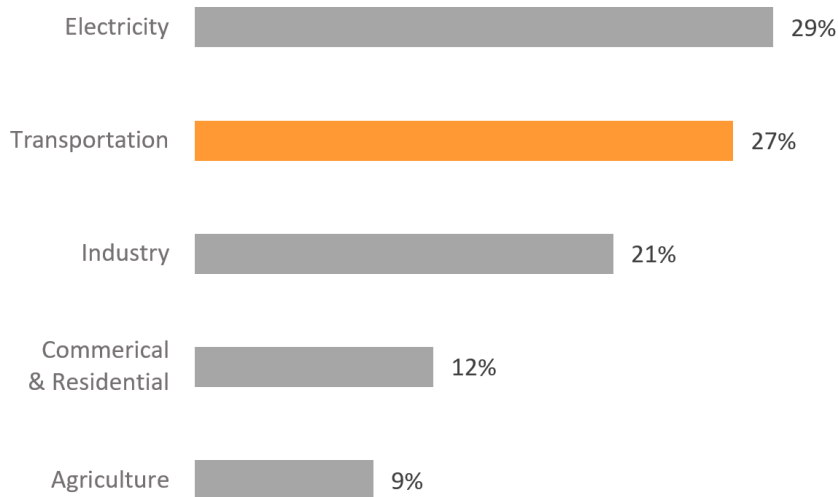


Figure 1.3: Breakdown of U.S. greenhouse gas emissions [3]

The FAA constructed a model analyzing the environmental impact from airplane emissions as a percent of the emissions level in 2005. Their models accounted for moderate, Fig. 1.4(a), and significant, Fig. 1.4 (b), advances in aircraft technology [4]. The black dashed line represents emissions, as a percent of the level in 2005, if no improvements are made, while the red dashed line represents the best possible outcome in reduced emissions from aircraft improvements. Even assuming significant technological advances, it is clear from Figure 1.4(b) that improvements to conventional airframe and engine design alone are not enough to reach goals of maintaining emission levels equivalent to those in 2005. Without innovative solutions to this problem, climate change will begin to have a catastrophic impact on the planet in the near future. Therefore aircraft need to be designed to minimize emission and fuel burn while increasing efficiency.

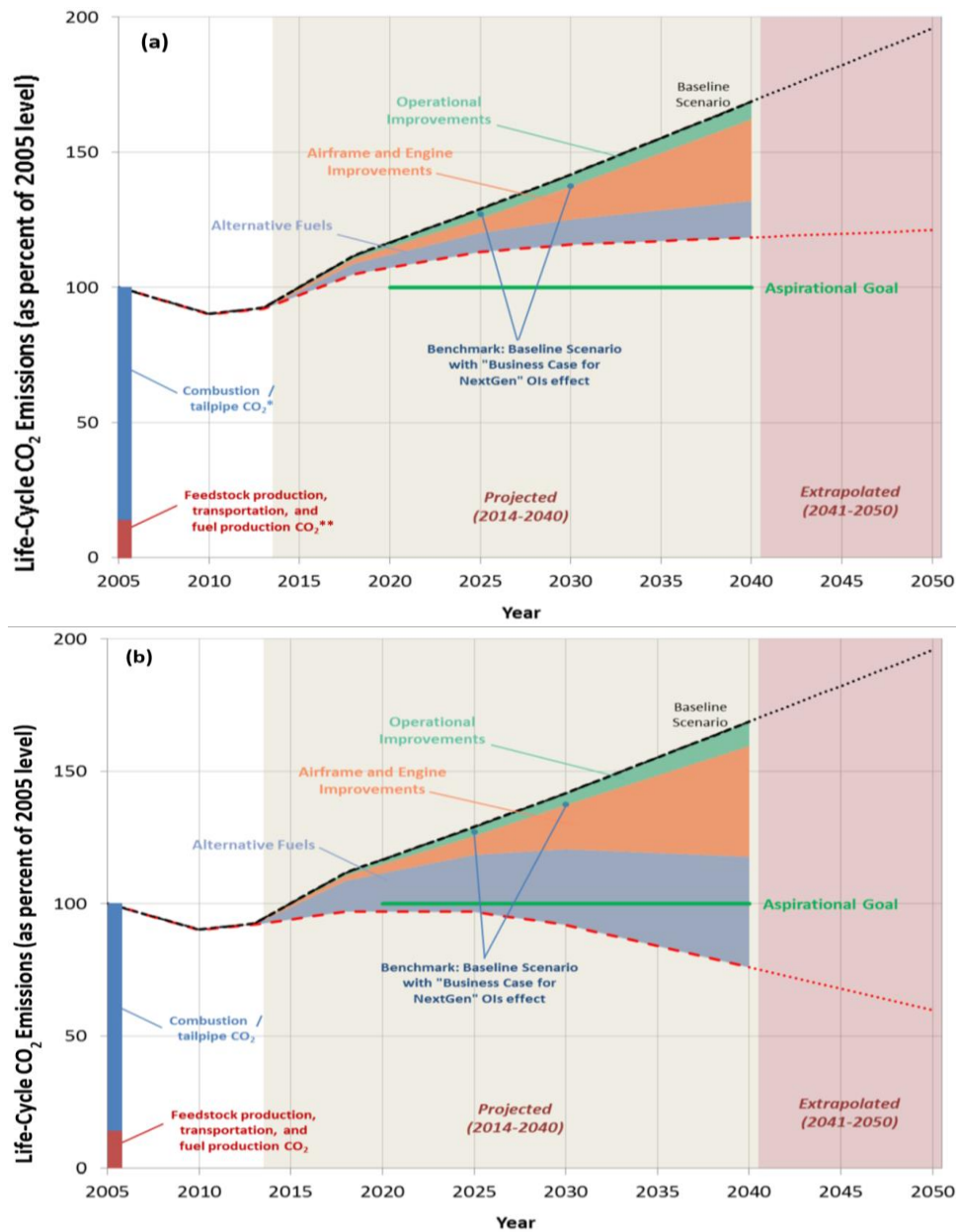


Figure 1.4: Projected environmental impact from CO₂ emissions with (a) moderate advances in airplane technology and (b) significant advances [4]

*combustion/tailpipe emissions are created by airline industry

**feedstock production, transportation, and fuel production emissions for conventional jet fuel are created from extraction and refinement

1.2 Future Aircraft Designs

NASA identified four areas of aircraft design in which they propose improvements, detailed in Table 1.1. By 2035, their goal is to reduce emissions by 75% and increase

performance by 70% [5]. In order to meet these goals, innovative airframes and propulsion systems need to be considered. One such concept is distributed propulsion, which distributes propulsive thrust along the span of the wing [6]. However, to reach emissions goals, turboelectric propulsion is being considered, in which electric generators provide power to motor driven fan blades, creating thrust.

Table 1.1 NASA's Goals for Aircraft Design (STOL)

| Corners of the trade space | (2015) Conventional Tube and Wing | (2020) Conventional Hybrid Wing Body | (2035) Advanced Aircraft Concepts |
|----------------------------|--------------------------------------|---|--------------------------------------|
| Noise (below stage 4)* | -32 dB | -42 dB | -71 dB |
| LTO NOx Emissions | -60% | -75% | >-75% |
| Fuel Burn | -33% | -40% | -70% |
| Field Length | -33% | -50% | Short Take-Off/Landing Concepts |

*see Fig. 2.1 for noise stages

1.3 Superconducting Machines

Conventional motors and generators, which rely on copper windings and iron cores are too heavy to be practical in airborne situations where weight is a critical design parameter, therefore requiring superconducting machines for turboelectric propulsion [7]. However, a major drawback of superconducting machines is that they must be operated at cryogenic temperatures, which requires substantial amounts of cooling power. When exposed to variable magnetic fields and variable currents (AC), superconductors experience AC losses which produce heat. Since operating temperatures can be as low as 4 K, equivalent to -269 °C, it is desirable to minimize these losses, reducing refrigeration power [8]. When designing superconducting machines, accurate calculations of AC losses

are paramount. However, in order for superconductivity to be feasible, AC losses need to be less than 0.1% of total power [5].

1.4 Problem Statement

A program, developed by Masson et al., sizes 3-D superconducting rotating machines [9]-[12]. The program consists of a low fidelity semi-analytical optimization function, referred to as SIZING, and high fidelity electromagnetic, thermal, and structural models, referred to as AMBER. SIZING produces a zeroth order model by minimizing machine mass while constraining AC losses and outputs the results for dimensions, mass, and AC losses which are then refined in AMBER.

The assumptions made in SIZING, in order to simplify loss calculations, resulted in large discrepancies between the low and high fidelity solutions. The zeroth order model is used as a basis for AMBER's calculations. While SIZING is not meant to be a high fidelity model, if inaccuracies are too large AMBER will not be able to produce the best solution since it is limited by SIZING's results.

Accurate loss calculations are necessary in order to optimize superconducting machines and develop the required cooling system. Unfortunately AC losses are notoriously difficult to calculate. Typically AC loss calculations use analytical equations, but these require strong assumptions (based on critical state model, critical current density independent of magnetic field) determine a solution, which can result in low accuracy. Alternatively numerical simulations can be used to determine the AC losses, but generally require significant amounts of computation time. A third method, implemented in this work is to use semi-analytical solutions and scaling laws based on numerical simulations [13].

The scope of this thesis focuses on correcting electromagnetic analysis in SIZING and AMBER, with a strong emphasis on improvements to SIZING by investigating the following questions:

- How does the inaccuracy of the low fidelity SIZING function affect the results from the high fidelity AMBER model?
- Where can modifications be implemented to improve accuracy of SIZING?
 - o How to improve magnetic field, AC loss, and machine volume calculations?
- How to correct AC losses in AMBER?
- How to implement correct magnetic field?
- Can SIZING be accurate enough to be a stand-alone program?
- Are fully superconducting machines better than partially superconducting machine? (superconducting stator vs. copper stator)

1.5 Thesis Structure

This thesis is divided into 5 chapters. Chapter 2, following this introductory chapter, focuses on background information pertinent to this work, reviewing conventional jet engines, turboelectric propulsion systems, basics of superconductivity, and AC loss mechanisms. Chapter 3 covers the model, first detailing aspects of how AMBER and SIZING work, then explaining the implemented improvements. Chapter 4 provides results and discussions on the accuracy of SIZING. Finally, chapter 5 presents the conclusions and suggested future work.

2. BACKGROUND

2.1 Current Aircraft Design

Over the past several decades, as air traffic increased, the FAA created regulations to reduce noise and fuel burn while improving efficiency. Aircraft noise limits are divided into four stages, the loudest is Stage 1 while the quietest is Stage 4. These limits are internationally recognized and must be met before an aircraft becomes operational. Currently larger aircraft must meet Stage 3 or 4 regulations and smaller aircraft must be below Stage 2 regulations [14]. Airframe improvements resulted in reduced noise levels, Fig. 2.1, but as aircraft size increases, in response to travel demands, it will be difficult to reduce noise levels further without revolutionary airframe designs [12].

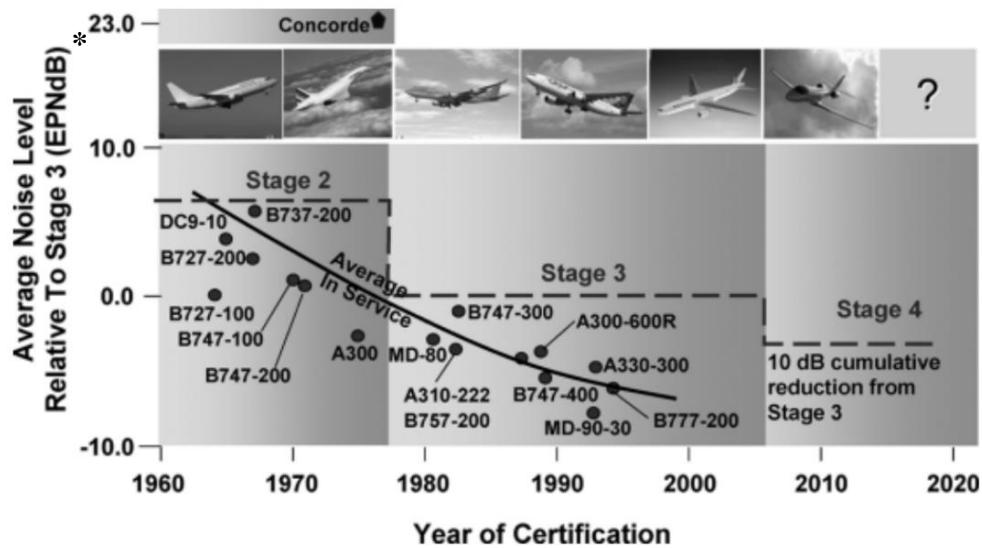


Figure 2.1: Reduction to aircraft noise level over the years[12]

*EPNdB: Effective Perceived Noise level in decibels

The design of more fuel efficient airframes and engines, specifically the invention of the high bypass ratio turbofan engine, improved aircraft fuel burn rates, shown in Fig. 2.2 [15]. The high bypass ratio turbofan engine creates propulsive thrust in most conventional airplanes. The ratio of the air stream passing outside the engine core to the

air stream passing through the core determines the bypass ratio. The higher the bypass ratio, the lower the exhaust speed, decreasing fuel burn and noise, while increasing propulsion efficiency and weight. However, the fan is typically connected to the turbine shaft, coupling the torque and speed of the engine to the turbofan tip speed. This limits the engine's efficiency, since turbines are more efficient at higher speeds [12]. However, the FAA's model in Fig. 1.4, suggests that without new approaches to engine design, the goals detailed by NASA in Table 1.1 are unlikely to be achieved [4], [5].

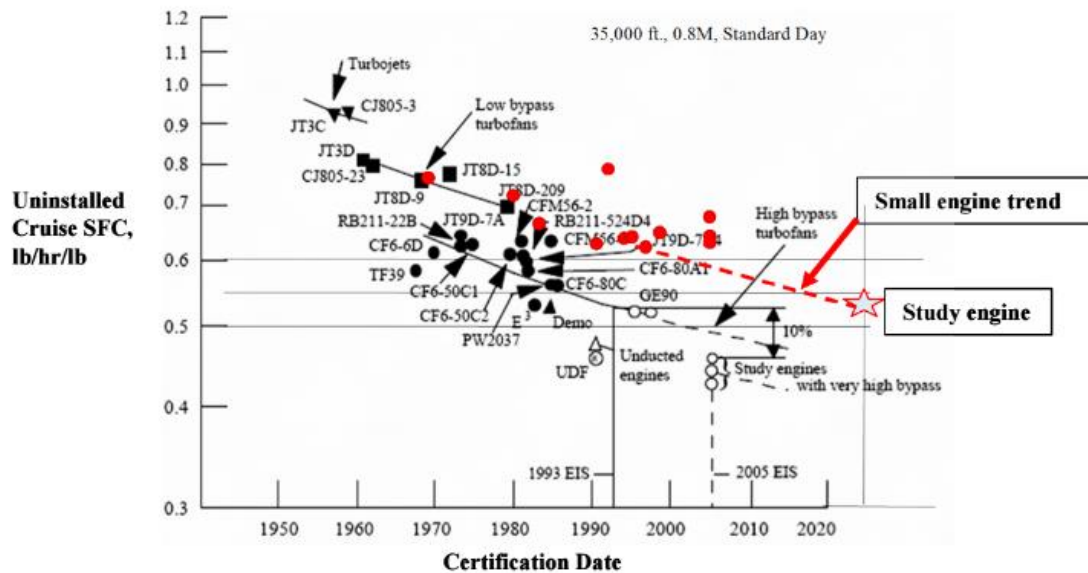


Figure 2.2: Reduction in fuel burn throughout the years [15]

2.2 Turboelectric Propulsion

In order to meet NASA's goals (Table 1.1), design concepts for distributed propulsion, investigated in [7], [5], [11], [12], [15]- [25], aim to reduce noise and takeoff and landing distances, while improving propulsive efficiency and fuel burn. Many distributed propulsion systems are based on a Hybrid Wing Body (HWB) or Blended Wing Body (BWB) aircraft design, which merges the fuselage with the wings and eliminates the tail, shown in Fig. 2.3. Multiple, small high bypass ratio engines are mounted on top of, or embedded in, the wings. This allows the exhaust to be vented along the wing's trailing edge,

filling in the wake and reducing drag, resulting in higher efficiencies. This shape allows for rapid climbs and steep descents equating to shorter takeoff and landing scenarios which decreases noise. Studies based on this concept have produced aircraft designs with improved fuel efficiency and lower noise [15]-[21].



Figure 2.3: HWB distributed propulsion conceptual design [19]

While innovative results show that distributed propulsion increases efficiency and reduces fuel consumption, generating thrust with high bypass ratio engines will not likely reduce emissions enough to meet NASA's requirements [5]. Therefore turboelectric propulsion, considered in [7], [5], [11], [12], [23]-[25], proposes that thrust be generated by multiple electric motor-driven fans, distributed along the wingspan. Generators, mounted on the wing tips, will deliver power to the motors via transmission lines, shown in Fig. 2.4.

Weight is a significant factor when considering electric motors and generators for propulsion in airplanes. Conventional machines, constructed with normal conductors such as copper, typically have power densities less than 1 kW/kg . In order to produce the power required to generate thrust, the machines become too massive for flight [12]. Therefore, superconducting machines are considered as an alternative. With typical power densities in the range of $10 - 20 \text{ kW/kg}$, superconducting machines are capable of producing the

necessary thrust while weighing much less than their conventional counterparts [7], [12], [24].



Figure 2.4: Distributed turbo-electric propulsion conceptual design [25]

A major advantage of electric propulsion is decoupling the power and propulsion. As previously mentioned, the fans are mechanically connected to the motors, which are electrically connected to the generators. The motors, limited by the fan tip speed, operate at lower speeds. While the generators, since they are electrically decoupled from the fan tip speed, are able to operate at higher speeds. Due to their quick response time, electric machines also allow for asymmetric thrust to produce pitch, yaw, and roll. Other benefits of electric propulsion include redundancy, if one motor is lost there are multiple others to carry the load, and easy maintenance when compared to the high maintenance hydraulic systems for gas turbine engines [5], [12], [24].

Some drawbacks for turboelectric propulsion include cryogenic temperatures, weight increases, and AC losses. Cryogenic temperatures are required for the operation of superconducting machines. Liquid hydrogen (LH2), has been proposed as a potential cooling system at 20 K, and fuel source for the turbo-generators [7], [5], [12]. While

superconducting machines are lighter than the alternative turbofan engine turbine cores, they require heavy cooling systems, increasing weight. In addition AC losses dissipate in the form of heat, increasing refrigeration requirements. The alternating fields experienced at the stator can produce large losses in superconductors. To limit these losses many superconducting machines are constructed with copper stators. However, advances in materials technology are leading to better superconductors less susceptible to AC losses. NASA predicts that, as long as AC losses can be constrained, using a superconducting stator would decrease machine mass [5].

2.3 Superconductivity

Superconductivity is a phenomenon by which certain materials exhibit no electrical resistance when cooled below a critical temperature, T_c . H. Kamerlingh-Onnes discovered superconductivity in 1911 while researching the electrical resistance of mercury at low temperatures. He discovered that the electrical resistance of mercury suddenly dropped to non-measurable values at a temperature of 4.15 K. In metals, the resistivity, ρ , is temperature dependent, decreasing with temperature to a base resistivity, ρ_0 , determined by material purity. In contrast, the resistivity of superconducting materials abruptly drops to zero when the temperature is below T_c , which varies depending on material. However, above T_c superconductors have higher resistivities than normal conductors, such as copper. Fig. 2.5 qualitatively plots resistivity against temperature for a normal and superconducting material [26]-[29].

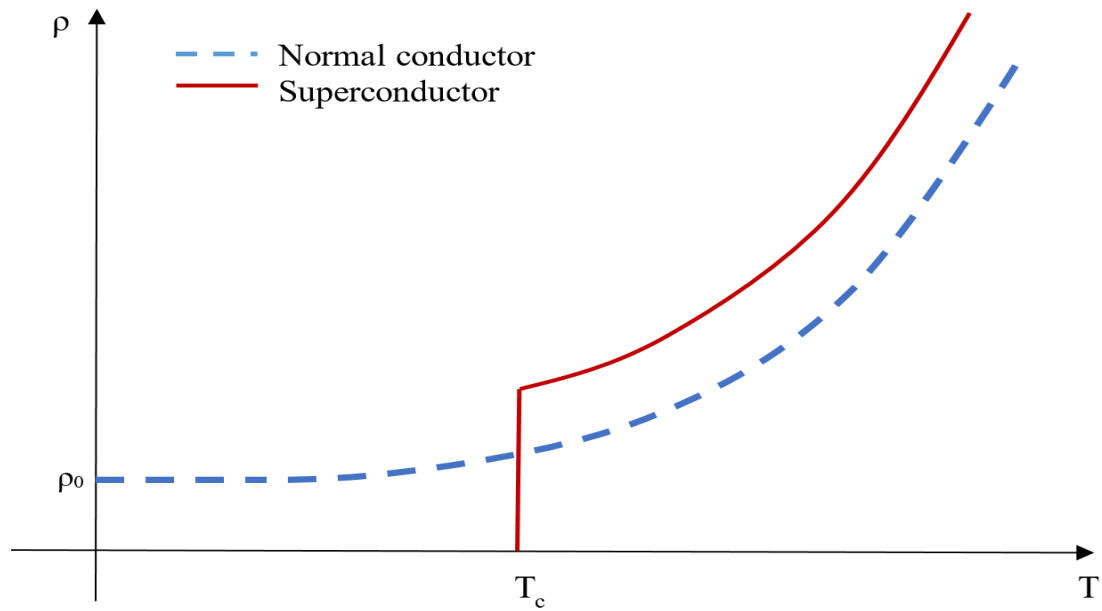


Figure 2.5: Qualitative plot of resistivity against temperature

Along with critical temperature, T_c , the transition to the superconducting state is determined by a critical magnetic field, B_c , above which superconductivity breaks down, and a critical current density, J_c . Transport current flowing through a superconductor generates a magnetic field. J_c is the current density above which the superconducting state is lost. The values of T_c , B_c , and J_c depend on each other as well as material properties. Thus the critical surface, formed by these three parameters, defines the transition from the normal to the superconducting state, shown in Fig. 2.6 [26].

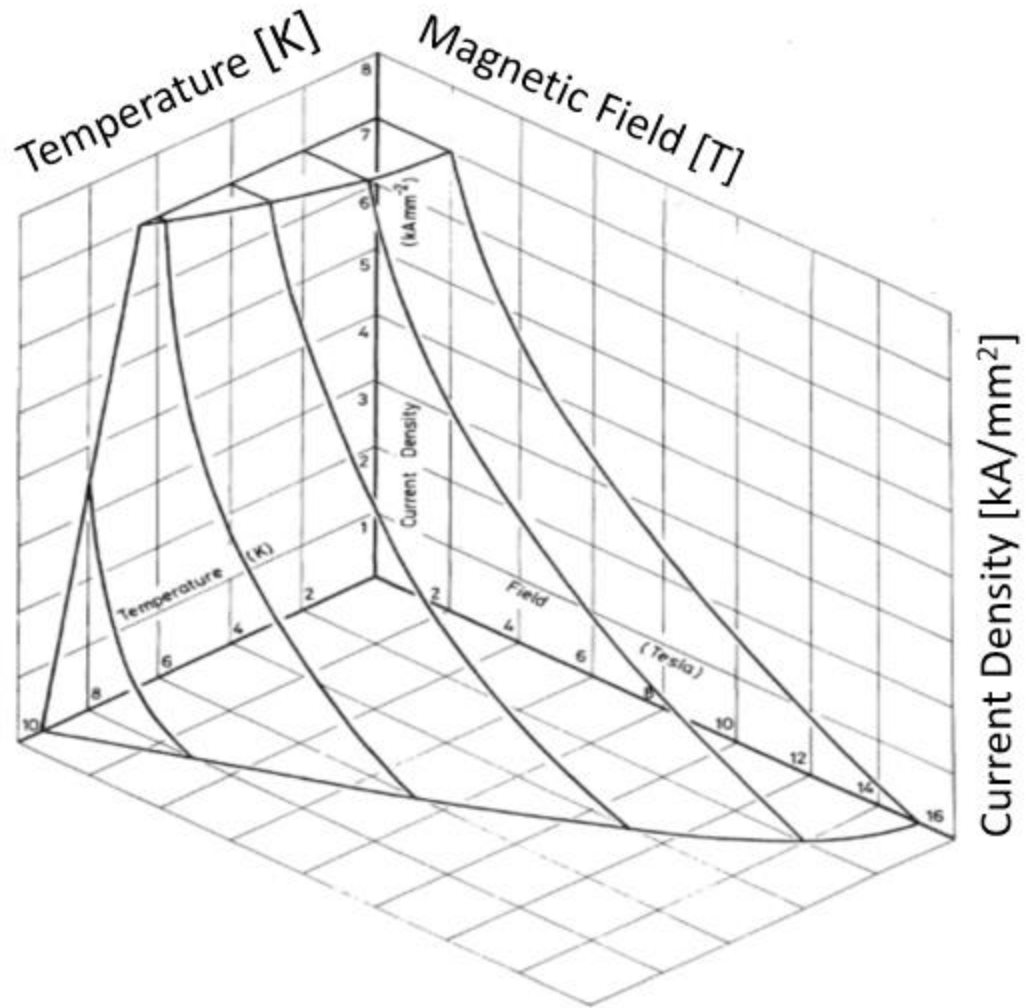


Figure 2.6: Critical surface for the superconductor niobium-titanium (NbTi) [26]

Another phenomenon presented by superconductivity is perfect diamagnetism below T_c . In the presence of an applied magnetic field, B_a , currents are generated on the surface of the superconductor shielding the inside from magnetic flux. This is known as the Meissner Effect, illustrated in Fig. 2.7. However, this is limited by B_c , above which, flux penetrates the interior and superconductivity breaks down. Superconductors that behave in this manner are defined as Type I, or soft, superconductors [26]-[29].

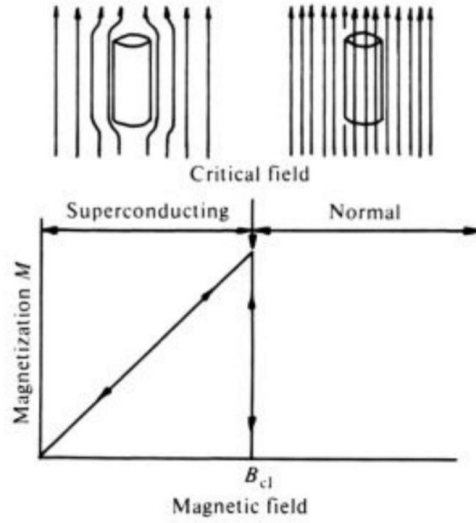


Figure 2.7: Meissner Effect in Type I superconductors [28]

Below T_c the applied field causes persistent currents to arise on the surface of the superconductor in order to screen, or cancel the flux inside. If flux is in the interior of the conductor while in the normal state, it is expelled upon transition to the superconducting state. The flux in the interior of the superconductor is represented by,

$$\mathbf{B} = 0. \quad (2.1)$$

Consequently, current cannot pass through the volume of the superconductor, instead it is forced to flow on the surface. From Maxwell's equations,

$$\nabla \times \mathbf{B} = \mu_0 \mathbf{J}. \quad (2.2)$$

If B is zero, then the curl of B must also be zero, thus J is zero. In reality, the current does not flow on the surface, but in a surface layer of thickness, λ , where the magnetic flux penetrates the conductor. Thus λ is called the penetration depth given by

$$\int_0^\infty \mathbf{B}(x) dx = \lambda \mathbf{B}(0). \quad (2.3)$$

Any current in the superconductor, screening and transport, must flow within this surface layer. Unfortunately, B_c is too low to allow for significant currents to flow, detailed in Table 2.1[28], [29].

Table 2.1: Critical Temperature and Field of Type I superconductors [28]

| Material | T_c [K] ($J = 0, B = 0$) | B_c [T] ($J = 0, T = 0$) |
|----------|---------------------------------|---------------------------------|
| Aluminum | 1.2 | 0.01 |
| Indium | 3.4 | 0.03 |
| Tin | 3.7 | 0.03 |
| Mercury | 4.4 | 0.04 |
| Lead | 7.2 | 0.08 |

Two critical fields characterize type II, or hard, superconductors, shown in Fig. 2.8. Below a lower critical field, B_{c_1} , they exhibit the Meissner effect and display perfect demagnetization, eliminating magnetic flux and current from their interior. However, above B_{c_1} flux begins to penetrate the interior through vortices allowing a quantum of flux to penetrate the material. Current flows around the vortices through the same penetration depth λ , when the external field increases, so does the density of the vortices allowing more magnetic flux to penetrate the superconductor. The material remains superconducting until it reaches an upper critical field, B_{c_2} , above which it becomes resistive. The creation of the vortex network and increase of the critical field, B_{c_2} , which is significantly higher than B_c in type I superconductors, allows type II superconductors to carry high current densities, making superconductors in high field electromagnetic applications possible. Table 2.2 details the high magnetic field and current densities tolerated in some common type II superconductors [28]. Conventional wires can tolerate about $10 A/mm^2$ with air cooling, whereas type II superconductors, of similar size, are capable of carrying thousands of A/mm^2 . Fig. 2.9 plots the critical current density and magnetic field for several different superconducting materials [26]-[28].

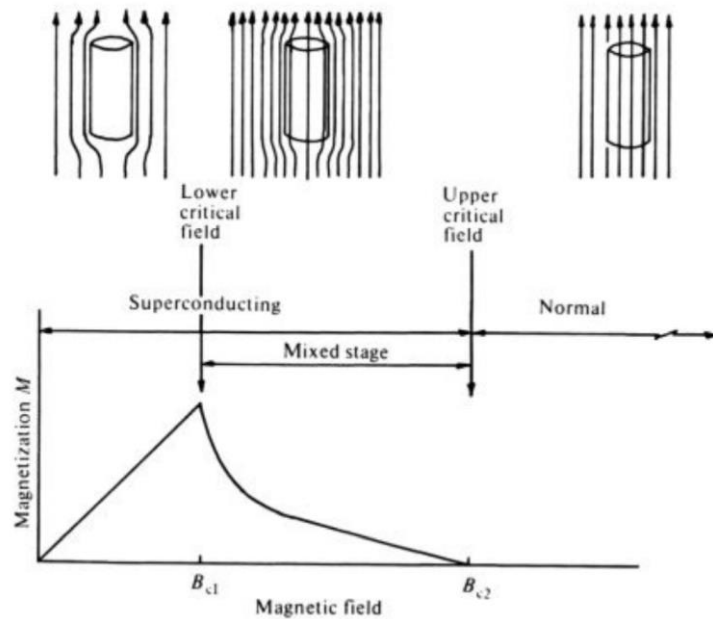


Figure 2.8: Magnetization of Type II superconductors, below B_{c1} they are perfectly diamagnetic, between B_{c1} and B_{c2} some flux is allowed to penetrate the conductor, above B_{c2} superconductivity breaks down [28].

Table 2.2: Critical Temperature, Field, and Current Density in Type II Superconductors [28]

| Material | T_c [K] | B_{c2} [T] at 4.2 K | Maximum B in use [T] | J_c [$\frac{A}{mm^2}$] at 4.2 K | |
|--------------------|-----------|-----------------------|------------------------|-------------------------------------|-----------------|
| | | | | $B = 4 T$ | $B = 10 T$ |
| NbTi | 10.2 | 12 | 8 | 15×10^3 | 2×10^2 |
| Nb ₃ Sn | 18.3 | 22 | 16 | 20×10^3 | 2×10^3 |
| V ₃ Ga | 16.5 | 22 | 20 | 6×10^2 | 6×10^2 |

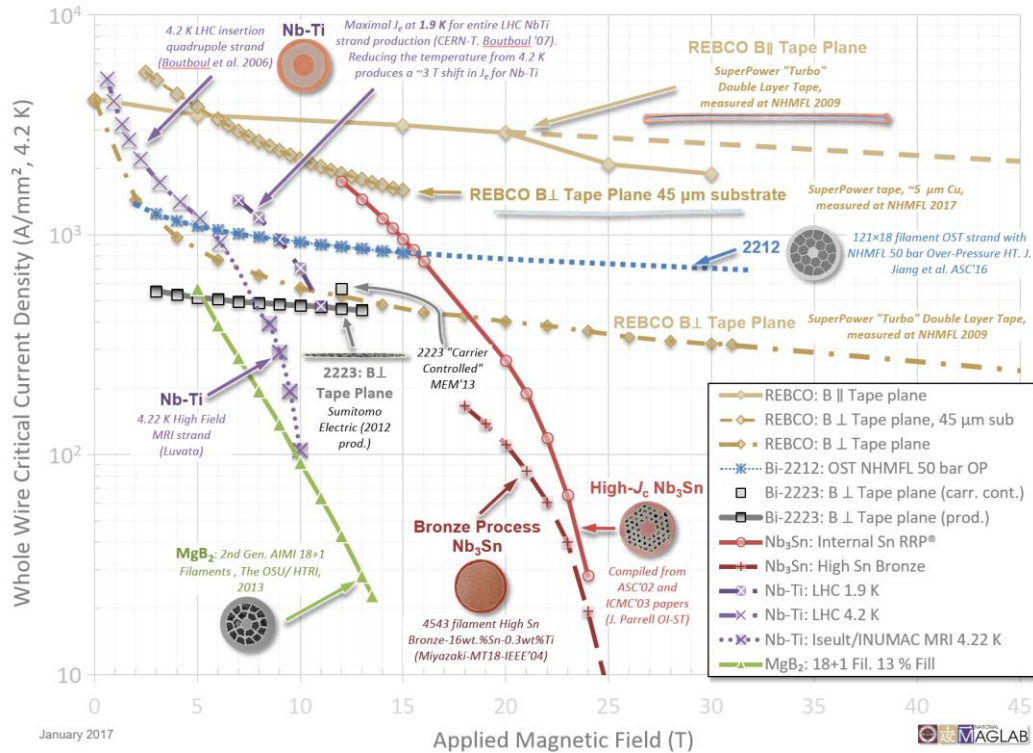


Figure 2.9: Critical current versus magnetic field for various superconducting materials[30]

Superconductors are also classified by their critical temperature. Low temperature superconductivity (LTS) superconductors typically have $T_c < 23 K$ and must be cooled with helium requiring significant cooling power. While high temperature superconductivity (HTS) superconductors have $T_c > 23 K$, with some of the copper-oxide superconductors having $T_c > 77 K$, the boiling point of liquid nitrogen and therefore lower refrigeration costs. Figure 2.10 shows T_c for various superconducting materials and the years they were discovered [26]-[29], [31]. The main power required for superconducting applications is the cooling power, which can be significant, thus HTS superconductors are advantageous, since they can greatly reduce cooling costs through operation at higher temperatures [8]. The work presented in this paper focuses on magnesium diboride, MgB₂, which is a Type II superconductor in between LTS and HTS superconductors with $T_c \approx 39 K$ [32].

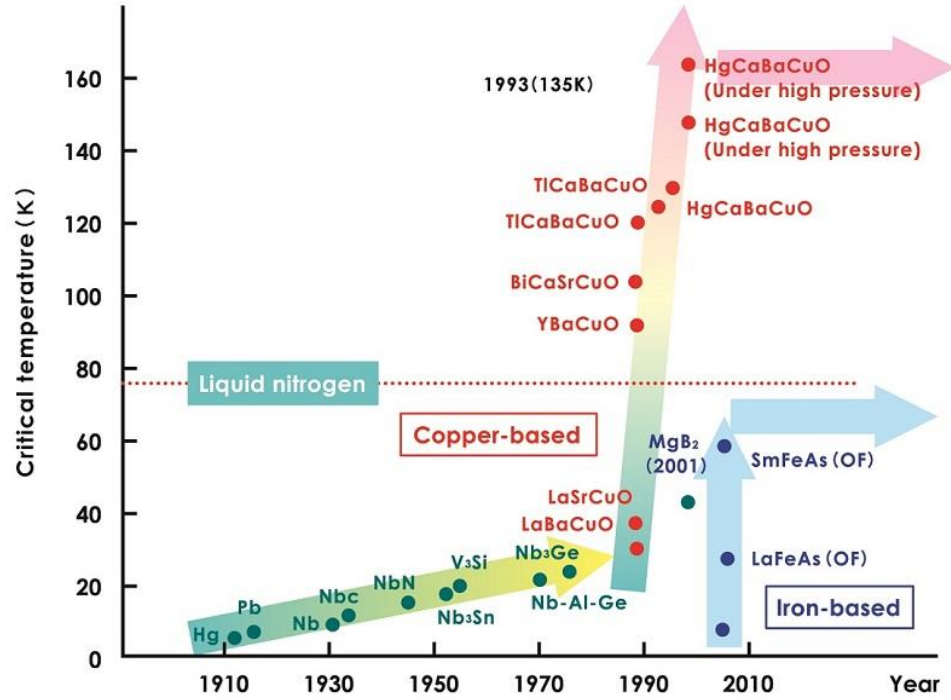


Figure 2.10: T_c of various superconducting materials [31]

2.4 AC Losses

Losses arise in superconductors due to time varying currents (AC) and time varying magnetic fields and are a concern primarily in Type II superconductors because electric fields can be produced within these materials [8]. According to Faraday's Law, a changing magnetic field produces an electric field given by Eqn. (2.4) [33]

$$\nabla \times \mathbf{E} = -\frac{\partial \mathbf{B}}{\partial t}. \quad (2.4)$$

Multiplying the electric field by the current density gives the power generated inside the superconductor as

$$P_g = \mathbf{E} \cdot \mathbf{J}, \quad (2.5)$$

which dissipates as heat [26]. In the presence of a changing field, superconductors are subject to hysteresis (magnetization), eddy current, and coupling losses. These AC losses

correspond to resistive losses, producing heat in the windings. Since superconductors operate at cryogenic temperatures, it is desirable to minimize losses, in turn reducing cooling power. In practice, to decrease losses, superconducting wires are made of composite materials containing fine, twisted superconducting filaments, with diameters on the order of tens of microns, embedded in a matrix material such as copper, Fig. 2.11.

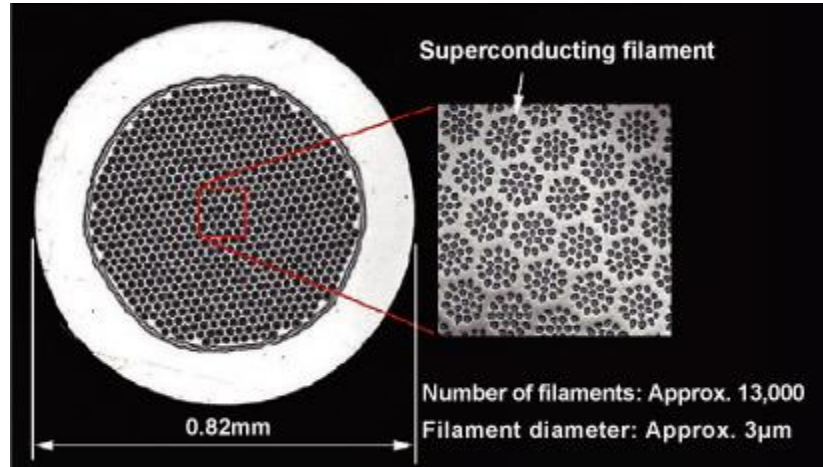


Figure 2.11: Superconducting filamentary composite wire [34]

2.4.1 Hysteresis Losses and the Critical State (Bean) Model

Consider a cylindrical superconductor in the presence of an applied magnetic field, B_a , perpendicular to its length as shown in Figure 2.12. In response to B_a , screening currents are induced on the surface to prevent magnetic flux from penetrating the interior of the superconductor, Fig. 2.12(a). Now it can be seen that the current density everywhere in the superconductor is assumed as either $J = 0$ or $J = J_c$.

Increasing the magnetic field by an amount ΔB causes the screening currents to increase, shielding the interior from changes in magnetic flux. Since the current density is already at J_c , increasing screening currents results in the magnetic flux penetrating deeper into the wire, Fig. 2.12(b), by a penetration depth $\lambda = \frac{2\Delta B}{\mu_0 J_c}$.

Another increase in magnetic field will result in the magnetic flux further penetrating the superconductor, Fig. 2.12(c). This process is repeated until the wire is fully penetrated by the magnetic flux, illustrated in Fig. 2.12(d). If the field is decreased by ΔB , the flux penetration does not recede, instead new currents arise to screen the inside from the changes in magnetic field, shown in Fig. 2.12(e)-(f). This creates a hysteresis cycle which can be shown by plotting the magnetic field, H , against the magnetization, M , shown in Fig. 2.13.

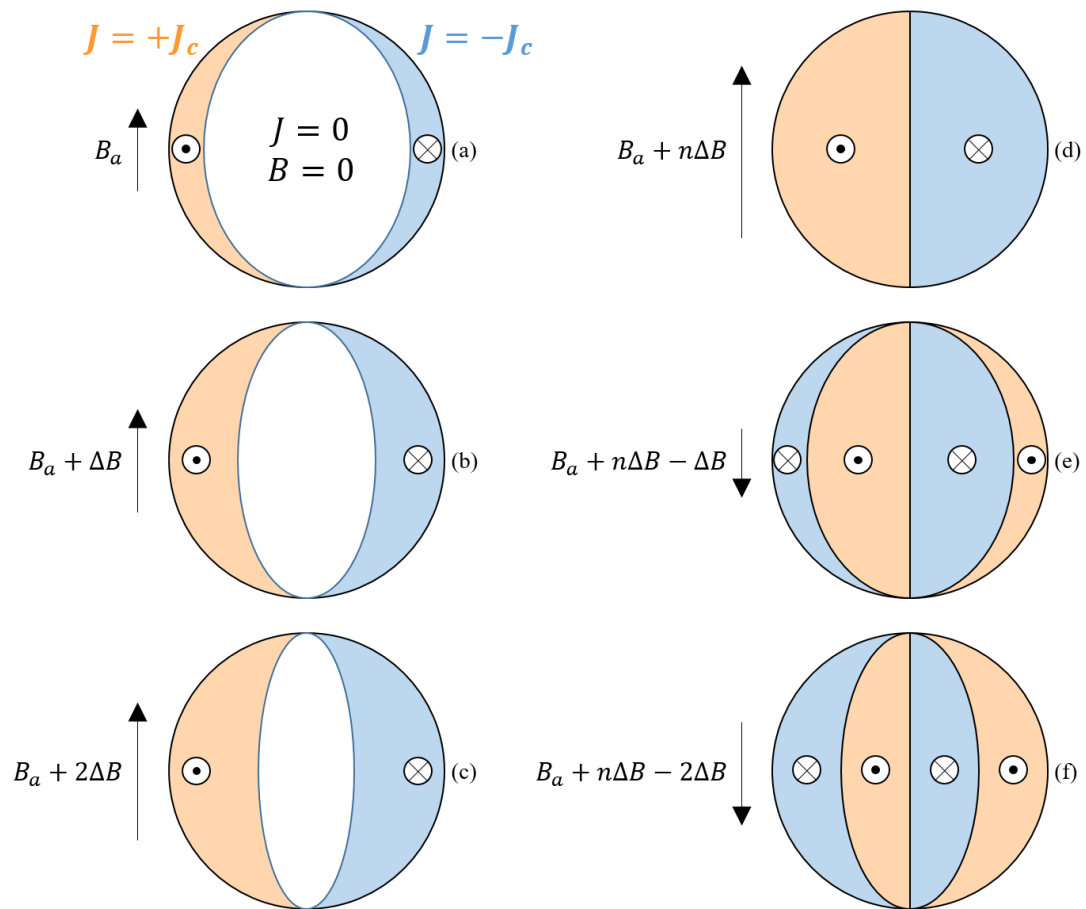


Figure 2.12: Screening Currents/critical state model

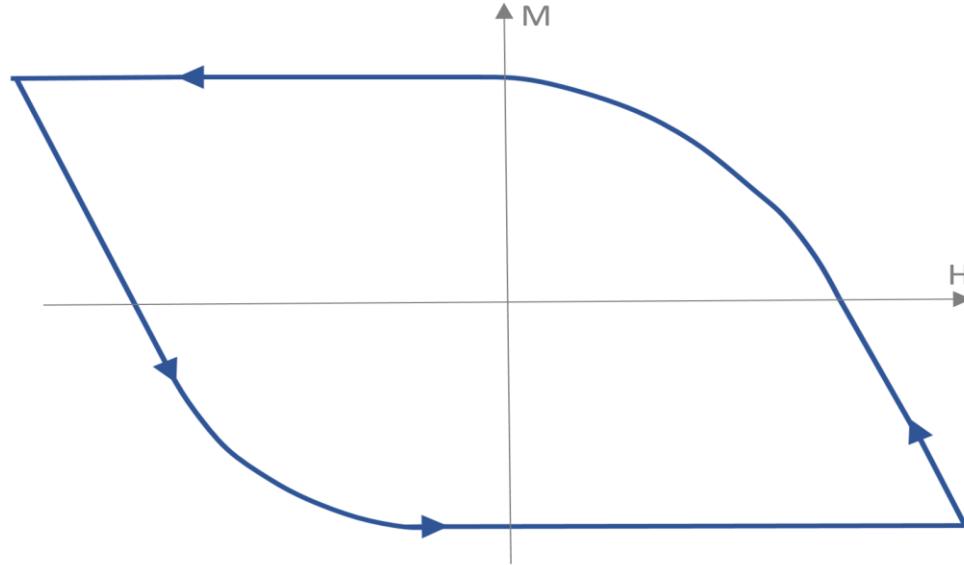


Figure 2.13: Qualitative hysteresis loop for a superconductor

This is known as the critical state or Bean model named after Bean, who developed the model in 1962 which makes the following assumptions [8], [26]:

1. The current density is in the direction of the electric field, \mathbf{E} .
2. The current density takes on only two values,

$$J = 0 \quad \text{or} \quad J = J_c \left(\frac{E}{E} \right).$$

3. J_c is independent of the magnetic field.

However, the value J_c depends on the magnitude of the magnetic field as shown by the critical surface in Fig. 2.6. There are two extensions of the Bean model that account for this field dependence. The first is the Kim model defining the critical current density as $J_c = \frac{\alpha}{B+B_0}$, where constants α and B_0 are determined for a fixed temperature. The second extension uses measured data to obtain $J_c(B)$ curves specific to each material [8]. An example of a $J_c(B)$ curve at 4.2 K for MgB_2 is represented by the green triangles in Fig. 2.9.

Hysteresis losses, also referred to as magnetization losses, are so called because they arise from magnetization of the superconducting filaments and are independent of frequency [8]. All solutions are based on the critical state (Bean) model. In general the hysteresis loss per unit volume per cycle can be determined by integrating over the hysteresis loop on Fig. 2.13 as [26],

$$Q = \int HdM = \int MdH. \quad (2.7)$$

Hysteresis losses have been analyzed for a variety of different situations, for further detail see [26] and [8]. The case of interest pertaining to this work is that of a cylindrical conductor, perpendicular to the alternating magnetic field, with alternating transport current. In this case, the inner boundary of the screening currents forms an ellipse as seen in Fig. 2.12. The corresponding loss per unit volume, for a circular conductor, detailed in [26] and [28], is

$$Q_H = \frac{8}{3\pi} J_c d_{fil} f B_m, \quad (2.8)$$

where d_{fil} is the diameter of a superconducting filament, f is the frequency, and B_m is the amplitude of the magnetic field.

When the conductor is carrying a transport current, the losses are increased by a factor of $\left(1 + \left(\frac{J_S}{J_c}\right)^2\right)$, where J_S is the transport current. Thus the hysteresis loss for a superconducting wire becomes [26], [28], [35]

$$Q_H = \frac{8}{3\pi} J_c d_{fil} B_m * \frac{f}{\pi \left(\frac{d_{fil}}{2}\right)^2} * \left(\frac{1}{1+M_{Cu-SC}}\right) * \left(1 + \left(\frac{J_S}{J_c}\right)^2\right) * V_{wire}, \quad (2.9)$$

where M_{Cu-SC} is the ratio of copper matrix to superconducting filaments in the composite wire and V_{wire} is the volume of the wire.

2.4.2 Coupling Losses

In order to reduce losses the superconducting filaments are twisted, forming loops as shown in Fig. 2.14. A changing magnetic flux, $\phi = \int \mathbf{B} \cdot d\mathbf{A}$, through a closed loop produces an emf, $\varepsilon = -\frac{d\phi}{dt}$. This emf drives current around the loops of twisted filaments, appearing to couple filaments together. The current flows along the centerline of a filament, then drops vertically through the composite to the filament beneath. The amount of losses produced depends on the amount of flux enclosed by a pair of filaments [35]. Twisting the filaments reduces the amount of flux a pair of filaments encloses [23]. The coupling loss in a filamentary composite wire is

$$Q_C = \frac{1}{4\rho} (f * TP * B_m)^2 * V_{wire}, \quad (2.10)$$

where TP is the filament twist pitch [8], [26].

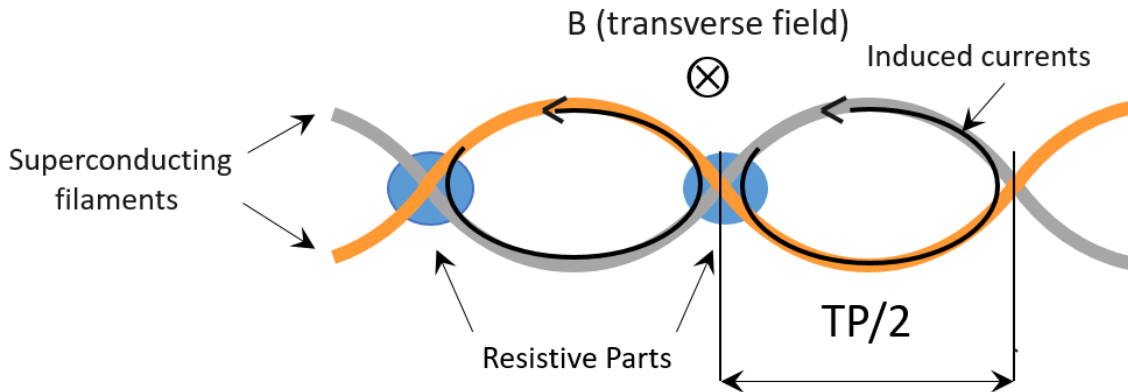


Figure 2.14: Coupling currents flows along filament then drops vertically through the composite to the opposite filament

2.4.3 Eddy Current Losses

In response to changes in the magnetic field Eddy currents are produced in the matrix material resulting in resistive losses. As defined by Bumby in [28] the eddy current loss in a superconducting wire is given by

$$Q_E = \frac{1}{4\rho} (\pi * f * B_m * d_{cond})^2 * V_{wire} * M_{Cu:SC}. \quad (2.11)$$

Detailed solutions for eddy current and coupling losses have been derived by Wilson using circuit analogy under the assumption that the superconducting filaments are fine enough to treat the composite as a homogenous, but anisotropic material [26]. While Carr provides a different approach, treating the composite as an anisotropic continuum and applying Maxwell's equations [8].

3. THE MODEL

Turboelectric propulsion for aircraft is a weight sensitive design process. The AC losses are important in determining the machine weight and efficiency of the system. As mentioned in the introduction a 3-D sizing model has been developed by [9]-[12] to determine the optimal design for superconducting rotating machines. The basic structure of the program is detailed in Fig. 3.1.

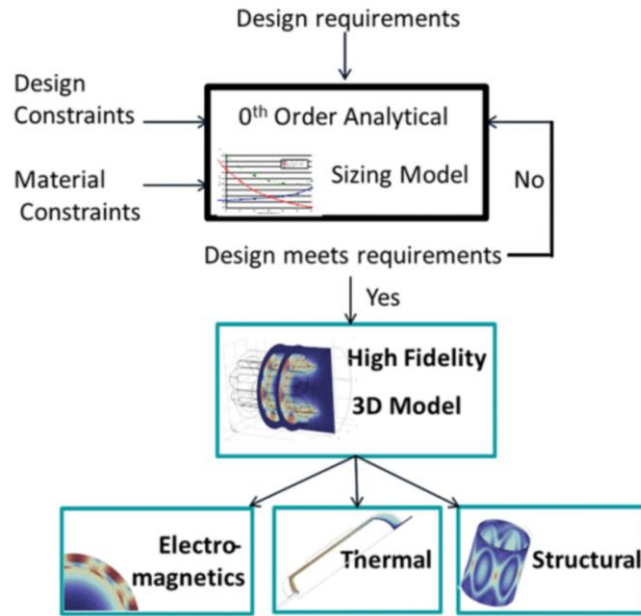


Figure 3.1: Basic structure of 3-d sizing program [9]

Given inputs for torque τ , power P , average stator radius r_0 , machine shapefactor L_a/r_0 , with L_a denoting the machine's active length, and stator electrical loading K_s , SIZING generates a zeroth order model, by minimizing the machine's active mass. The model outputs include machine geometry, AC losses, K_s , the no load magnetic field B_0 , L_a , and P . Then AMBER generates a 3-D mesh from SIZING's results and adjusts currents to eliminate magnetic field and torque discrepancies between the analytical and actual geometry. 3-D electromagnetic, structural, and thermal models then determine losses, inductance, heat leak, temperature distributions, and mass among other parameters.

The research presented here focuses mainly on the electromagnetic analysis with emphasis on improving the analytical solutions in SIZING. Therefore only a brief overview of AMBER's electromagnetic model is given. For further details on AMBER please see [9]-[12].

3.1 Overview of Electromagnetic Model in AMBER

The 3-D geometry for the electromagnetic model, Fig. 3.2, consists of the rotor, stator, and back iron. The rotor is composed of racetrack coils wound from superconducting tape, while multi-filamentary MgB₂ wires, wound into saddle coils, form the stator windings [9].

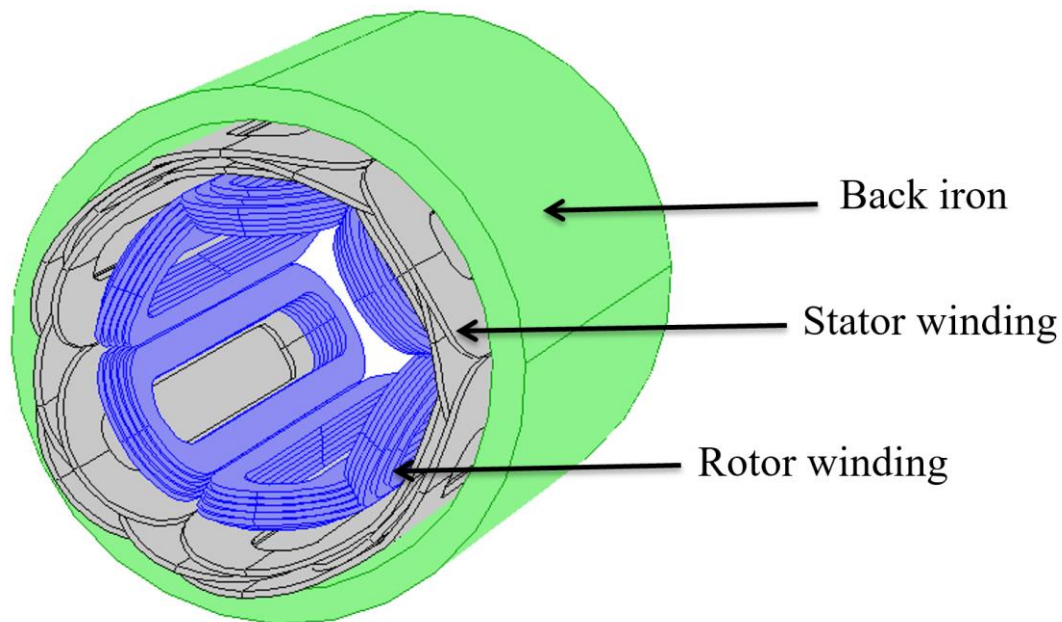


Figure 3.2: 3-D machine geometry [9]

Monte Carlo integration is a probabilistic method for numerical integration relying on random number generation to determine a solution. Implementing Monte Carlo integration, the magnetic field, produced by current sources, is calculated from the Biot-Savart Law given by,

$$\mathbf{B} = \frac{\mu_0}{4\pi} \iiint \frac{\mathbf{J} \times \mathbf{r}}{r^2} dV. \quad (3.1)$$

Simulating a rotation at full load, the variations in magnetic flux density and critical current for each conductor in one phase of the stator are recorded. From this data, the AC losses are calculated for each conductor [9]. The hysteresis losses are calculated based on the maximum field in each conductor. However, the difference in magnetic flux density, $dB = B_{max} - B_{min}$ [T], is used to determine the coupling and eddy current losses, calculated for each conductor by Eqns. (2.11) and (2.12), respectively [9].

3.2 Structure of SIZING

SIZING uses a gradient based optimization function to minimize the weight of a generic, air cored, rotating machine with an iron environmental shield, while placing constraints on the losses and machine dimensions. Fig. 3.3 details important parameters calculated in SIZING to determine the active mass of the machine, which consists of the rotor windings, stator windings, and back iron.

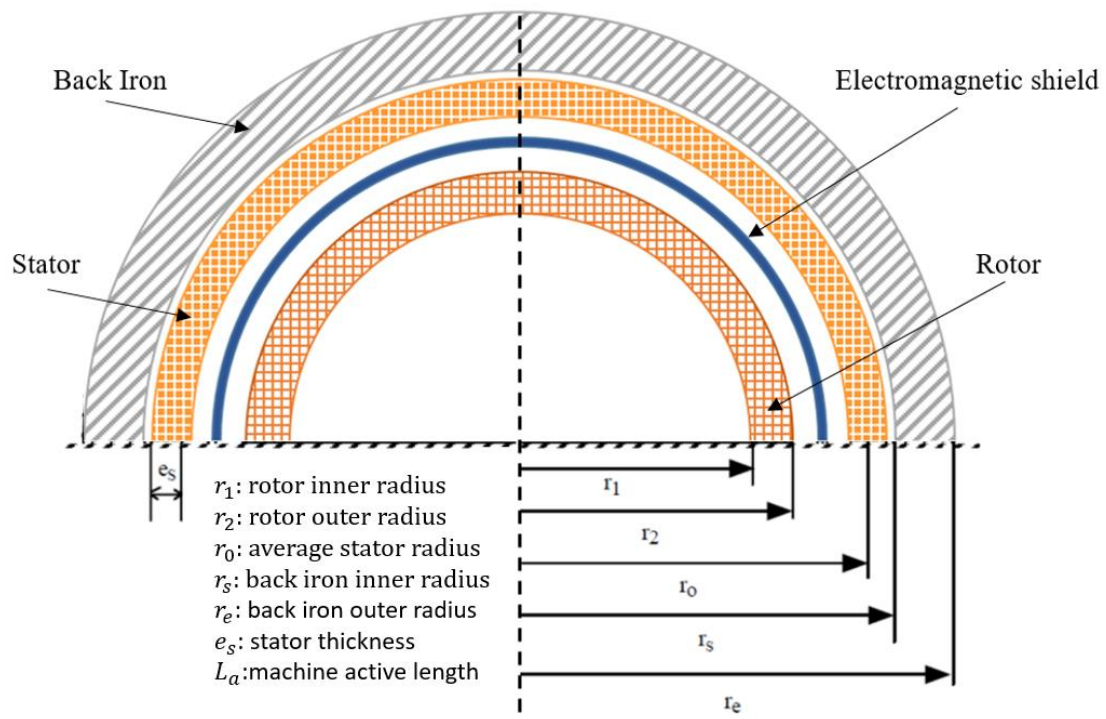


Figure 3.3: Basic machine geometry and important parameters calculated in SIZING

In addition to the active mass dimensions, highlighted in Fig. 3.3, SIZING also determines the geometry and mass for the machine's support structure. A few of these parameters, depicted in Fig. 3.4, include the rotor and stator support structures, the cryostat, and the shaft, located inside the rotor support structure.

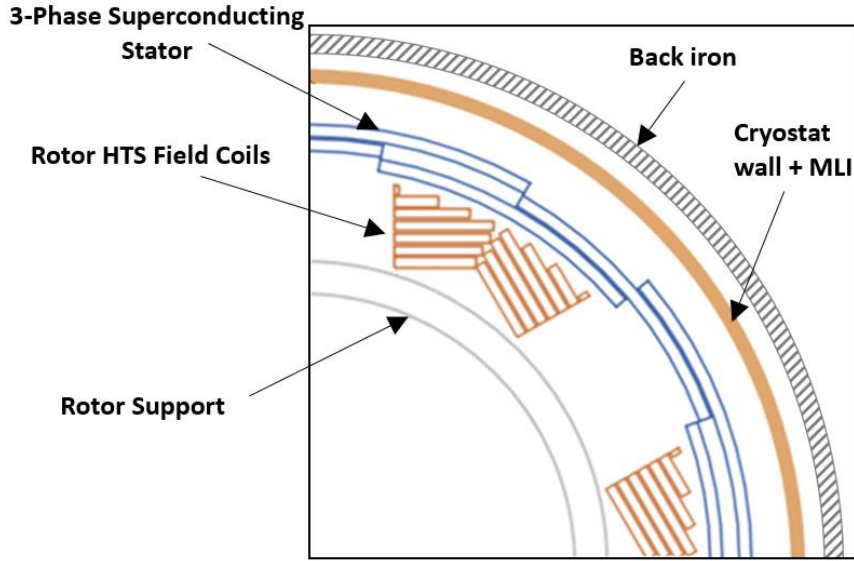


Figure 3.4: A 2-D cross section of the geometry, determined in SIZING, depicts a few of the structural parameters. MLI stands for multi-layer insulation and is used to reduce heat loss due to radiation

The user defines the machine power, P , in kW , speed in rpm , and stator material. Currently material properties are defined for copper, Cu, and MgB_2 . While the optimization function randomly generates values for the average stator radius, r_0 [m], the stator electrical loading, K_s [A/m], and the machine shapfactor, $SF = \frac{L_a}{r_0}$, where L_a is the machine's active length.

The necessary torque, τ , produced by the relation between the no load magnetic field, B_0 , and the electrical loading of the stator, K_s , is determined from the power by

$$\tau = \frac{P}{\omega} \text{ [Nm/s] ,} \quad (3.2)$$

where $P = \tau\omega$ and $\omega = \frac{2\pi * rpm}{60}$. The no load magnetic field, B_0 , can be determined from the torque by Eqn. (3.3). B_0 is the radial component of the magnetic field produced by the rotor at the radius r_0 , required to produce the torque defined in Eqn. (3.2) [10], [28]

$$B_0 = B_{RT_r}(r = r_0) = \frac{\tau}{\sqrt{2}K_s\pi r_0^2 L_a}. \quad (3.3)$$

The critical current, which depends on the magnetic field and operating temperature, T_{op} , taken as 20 K, is determined by Eqn. (2.5). For safety purposes, superconductor windings always operate at a fraction of their critical current, shown in Fig. 3.5.

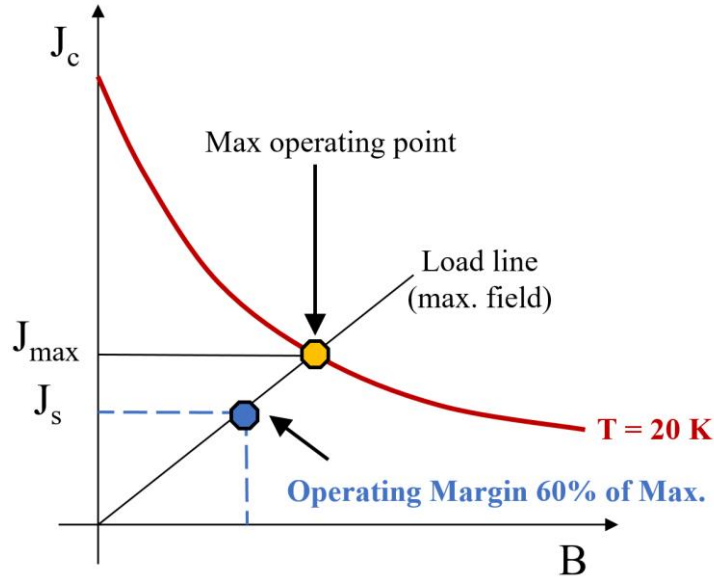


Figure 3.5: Qualitative plot of operation point compared to the maximum, or critical point.

From the dimensions outlined in Fig. 3.3 and the parameters derived above, the mass of the stator, rotor, and back iron are calculated. Of particular interest is the weight of the stator, necessary for computing losses, defined by

$$W_{St} = D_{St} * St_{fill} * V_{St} = D_{St} * St_{fill} * 2\pi r_0^2 * es * \left(\frac{L_a}{r_0} + \frac{5\pi^2}{12p} \right) [kg], \quad (3.4)$$

where V_{St} is the volume of the stator, D_{St} is the density of the stator conductor, and St_{fill} is the filling factor of the stator winding.

For simplified analysis the following assumptions were made when calculating the AC losses:

- Stator only experiences a purely alternating, transversely applied magnetic field
 - o Rotating component of magnetic field neglected
- Only the no load magnetic field, B_0 , contributes to the losses
 - o stator self-field neglected

AC losses were determined using analytical solutions to the critical state model in a purely alternating, transversely applied magnetic field, Eqns. (2.10)-(2.12). Adapted to a superconducting stator the loss equations become,

$$Q_H = \frac{8}{3\pi} J_c d_{fil} B_0 * \frac{f}{\pi \left(\frac{d_{fil}}{2}\right)^2} * \left(\frac{1}{1+M_{Cu-SC}}\right) * \left(1 + \left(\frac{J_S}{J_c}\right)^2\right) * V_{St}, \quad (3.5)$$

$$Q_C = \frac{1}{4\rho} (f * TP * B_0)^2 * V_{St}, \text{ and} \quad (3.6)$$

$$Q_E = \frac{1}{4\rho} (\pi * f * B_0 * d_{cond})^2 * M_{Cu.SC} * V_{St}. \quad (3.7)$$

The volume of the wire, V_{wire} , is simply exchanged for the stator volume,

$$V_{St} = 2\pi r_0^2 es \left(\frac{L_a}{r_0} + \frac{5\pi^2}{12p}\right). \quad (3.8)$$

The loss calculations only consider the magnetic field contribution from B_0 , as seen in Eqns. (3.5) – (3.7). Neglecting the effect of the stator self-field leads to inaccurate solutions and large discrepancies in the total AC losses, Eqn. (3.9), determined by SIZING and AMBER,

$$Q_{Tot} = Q_H + Q_E + Q_C. \quad (3.9)$$

The high fidelity AC losses solutions, produced in AMBER, are much smaller than the initial, low fidelity losses, calculated in SIZING. These large differences in loss solutions are shown in Figs. 3.6 - 3.9. The percent error between low and high fidelity solutions is calculated as

$$\% \text{ Error} = \frac{|AMBER - SIZING|}{AMBER} * 100\%. \quad (3.10)$$

The average percent error for the total AC losses was 158% with a maximum of 259% error. The simplifications led to significant errors in the hysteresis (Fig. 3.7) and eddy current (Fig. 3.8) losses with percent errors up to 429% and 692%, respectively.

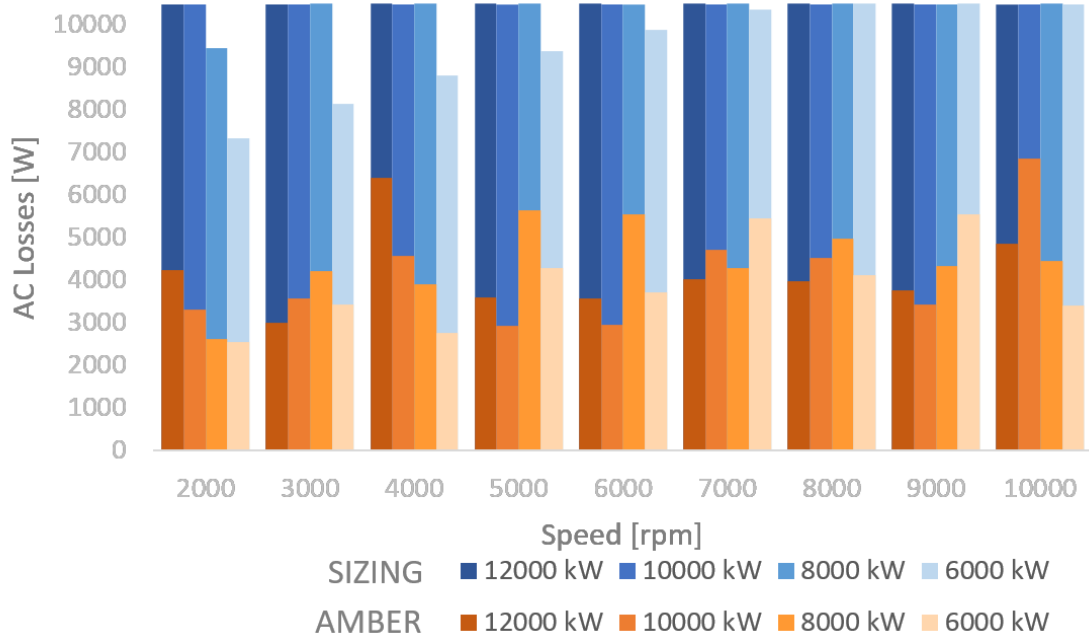


Figure 3.6: Difference in AC losses calculated in SIZING (blue) and AMBER (orange), with the respective percent error labeled for each case.

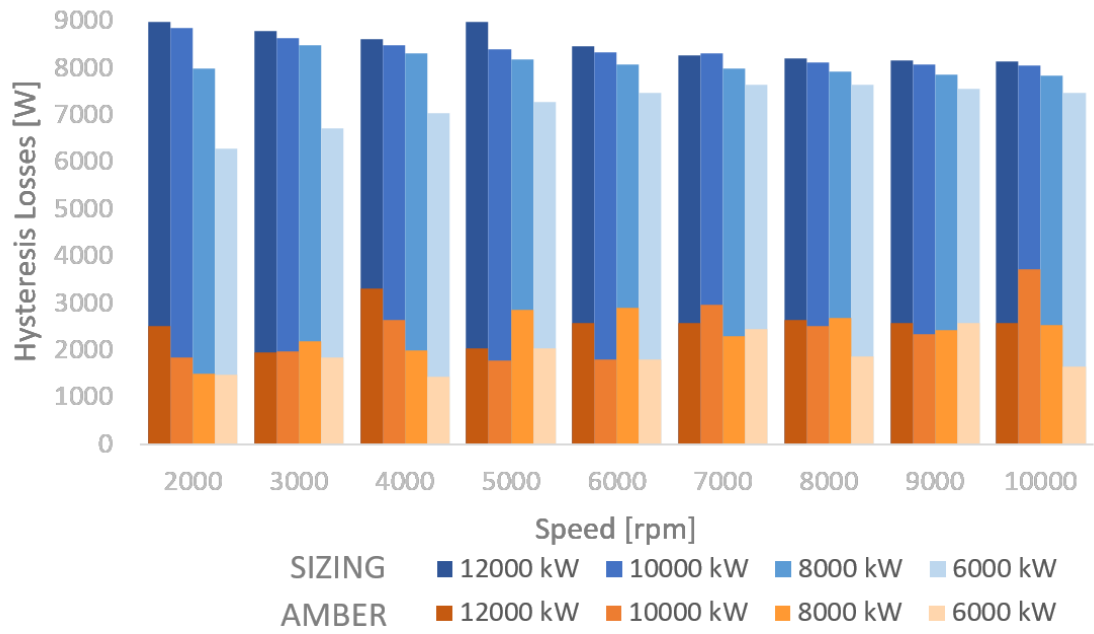


Figure 3.7: Difference in hysteresis losses calculated in SIZING (blue) and AMBER (orange), with the respective percent error labeled for each case.

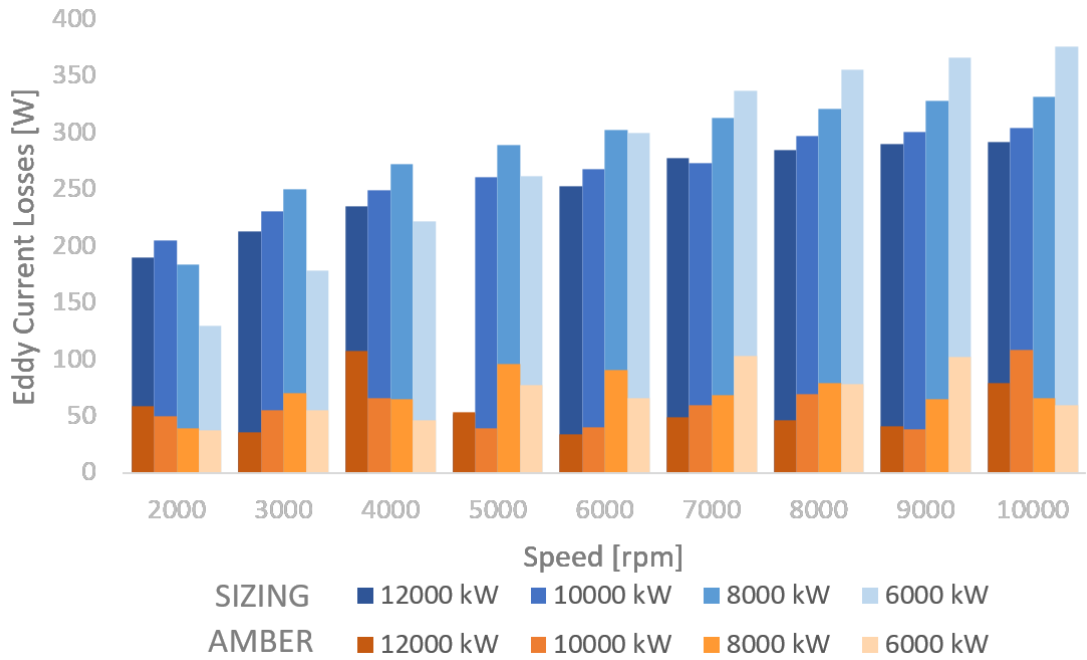


Figure 3.8: Difference in eddy current losses calculated in SIZING (blue) and AMBER (orange), with the respective percent error labeled for each case.

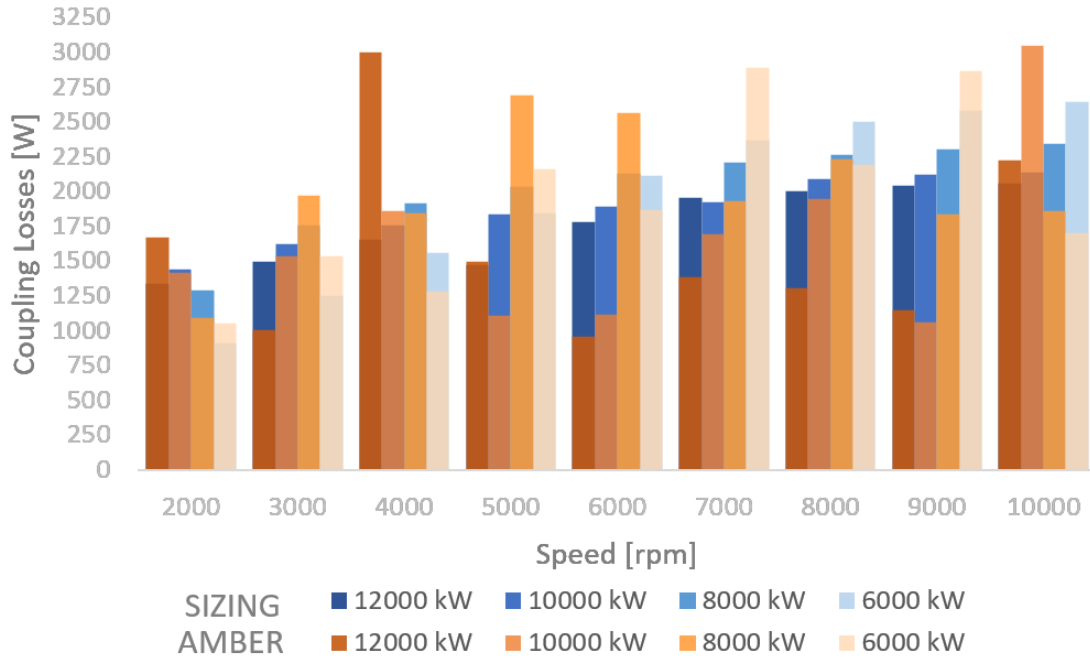


Figure 3.9: Difference in coupling losses calculated in SIZING (blue) and AMBER (orange), with the respective percent error labeled for each case.

The AC losses are inversely proportional to machine size, that is, as the machine size decreases the losses increase. Since B_0 is proportional to $1/r_0^2$, from Eqn. (3.3), the no-load magnetic field will increase as the average radius of the stator, r_0 , decreases. As B_0 increases, the losses will increase since Q_H is proportional to B_0 , from Eqn. (3.5), and Q_E, Q_C are proportional to B_0^2 , from Eqns. (3.6) and (3.7), respectively. Therefore, as SIZING minimizes the machine mass, the losses will increase until reaching the maximum losses constrained to 10500 W for this study. This prevents SIZING from further reducing machine mass, thus producing a solution with the AC losses maxed out at 10500 W. However AMBER calculates significantly lower losses, Figs. 3.6-3.9, signifying that SIZING is grossly overestimating the losses. This overestimation prevents SIZING from properly minimizing machine mass and, since AMBER's solution depends on SIZING's results, therefore, preventing AMBER from determining the best solution.

3.3 SIZING Improvements

Changes to SIZING include updated equations for the stator winding volume, the peak magnetic field in the stator, and AC losses. Additionally, adjustments were made allowing the stator to be set as either superconducting MgB₂ or copper. Finally, reprogramming SIZING allows it to be a stand-alone, analytical model to determine the size of rotating machines.

3.3.1 Stator Volume Calculation

Saddle coils, arranged in three phases, compose the stator winding. AMBER calculates the volume of each saddle coil, considering both the straight and curved portions of the coil, see Fig. 3.10. Whereas, SIZING roughly estimates the volume of the stator as a cylindrical tube with curved ends, Eqn. 3.8, with the term, $5\pi^2/12p$, accounting for the coil ends. Since AC losses depend on the stator volume, increasing the precision in SIZING's calculation will decrease error. SIZING's volume calculation was improved by approximating the calculations from AMBER.

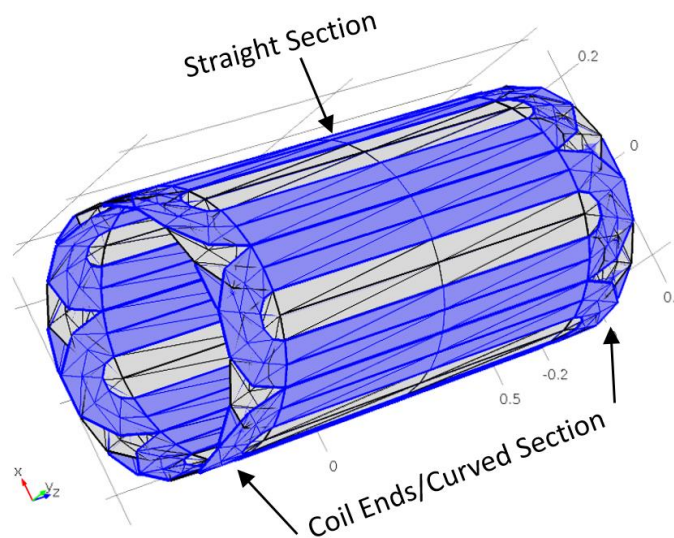


Figure 3.10: Stator showing 3 phases of saddle coils denoting the coil ends and straight sections of the coils

The volume, calculated in AMBER, for each phase is

$$V = \left[2p * \frac{2(\theta_1 - \theta_{saf})}{2\pi} * \left(\pi \left((Ri_{St-ph} + e_{St})^2 - (Ri_{St-ph})^2 \right) \right) * L_a \right] + \left[2p\pi \left(\left(\frac{d_1}{2} \right)^2 - \left(\frac{d_2}{2} \right)^2 \right) e_{St} \right]. \quad (3.11)$$

The first bracketed term determines the volume of the straight portion and the second bracketed term calculates the curved portion. Ri_{St-ph} is the actual inner radius of each phase of saddle coils given by, $Ri_{St-ph} = Ri_{St} + phase(e_{St} + istst)$, where e_{St} is the width of one phase and $istst$ is the spacing between two phases. $d_1 = \left(Ri_{St-ph} + \frac{e_{St}}{2} \right) \theta_1$ and $d_2 = \left(Ri_{St-ph} + \frac{e_{St}}{2} \right) \theta_2$ are the outer and inner diameters of the curved portion of the coil, respectively, where $\theta_2 = \frac{(2\pi)}{3p}$ and $\theta_1 = 3\theta_2 - \theta_{saf}$, see Fig. 3.11. The total volume of the stator is determined by adding the volumes of each phase.

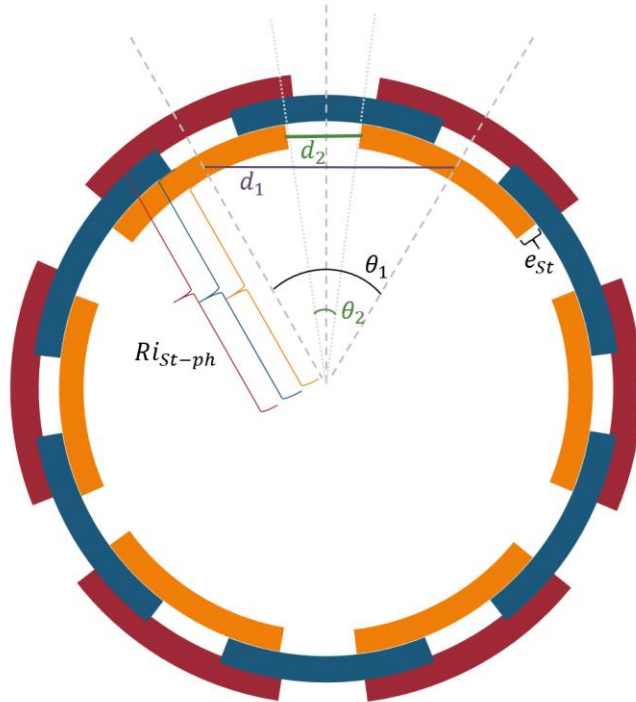


Figure 3.11: Parameters used in calculation of saddle coil volume

The term, $Ri_{St-ph} + \frac{e_{St}}{2}$, present in the definitions of d_1 and d_2 , is the average radius for each phase, which for the middle phase is approximately r_0 . Then from Eqn. 3.11, the volume for the middle, or second, phase, in terms of r_0 becomes

$$V = \left[2p * \frac{2(\theta_1 - \theta_{safe})}{2\pi} * \left(\pi \left(\left(r_0 + \frac{e_{St}}{2} \right)^2 - \left(r_0 - \frac{e_{St}}{2} \right)^2 \right) \right) * L_a \right] + \left[2p\pi \left(\left(\frac{r_0\theta_1}{2} \right)^2 - \left(\frac{r_0\theta_2}{2} \right)^2 \right) e_{St} \right]. \quad (3.12)$$

The first bracketed term in Eqn. 3.12 simplifies to $\frac{2}{3}\pi r_0 e_{St} L_a$, one third the volume of a cylindrical tube. Multiplying this volume by 3 accounts for each phase, assuming that each phase is of similar volume. Therefore calculating the volume of a cylindrical tube, by $\frac{2}{3}\pi r_0 e_s L_a$, where $e_s \approx 3e_{St}$, gives a good approximation for the volume of the straight portion of conductors.

The difficulties occur when calculating the volume of the curved conductors at the coil ends. SIZING calculates the volume of the coil ends for the middle phase by replacing e_{St} with $e_s/3$ in the second bracketed term of Eqn. 3.12. Multiplying this value by 3 accounts for each phase resulting in a volume of $3 * \left[2p\pi \left(\left(\frac{r_0\theta_1}{2} \right)^2 - \left(\frac{r_0\theta_2}{2} \right)^2 \right) \frac{e_s}{3} \right]$. Thus the volume for the stator can be approximated by

$$V_{St} = \frac{2}{3}\pi r_0 e_s L_a + 3 * \left[2p\pi \left(\left(\frac{r_0\theta_1}{2} \right)^2 - \left(\frac{r_0\theta_2}{2} \right)^2 \right) \frac{e_s}{3} \right], \quad (3.13)$$

which simplifies to,

$$V_{St} = 2\pi r_0^2 e_s \left(\frac{L_a}{3r_0} + \frac{2\pi^2}{9p} \right). \quad (3.14)$$

3.3.2 Magnetic Field Corrections

Hysteresis, Eddy Current, and Coupling losses all depend on the magnetic field, which needs to be properly calculated in order to accurately analyze losses. Previously, the only field considered in the loss analyses was the no load magnetic field, Eqn. (3.3), which was assumed to be purely alternating. However, in a motor or generator, the stator experiences an elliptical magnetic field, defined as the linear combination of rotating and out-of-phase alternating magnetic fields, given by

$$\mathbf{B}_{rot} = \mathbf{B}_\theta = \begin{cases} B_x \\ B_y \end{cases} = \begin{cases} kb_0 \sin(\omega t) \\ kb_0 \cos(\omega t) \end{cases} \text{ and} \quad (3.15)$$

$$\mathbf{B}_{alt} = \mathbf{B}_r = \begin{cases} B_x \\ B_y \end{cases} = \begin{cases} 0 \\ (1-k)b_0 \cos(\omega t + \varphi) \end{cases}, \quad (3.16)$$

where b_0 is the magnitude of the magnetic flux density [T], φ is the phase angle between the rotating and alternating magnetic field components, and k is the field ellipticity, ranging from 0 to 1, where 0 defines a purely alternating field and 1 defines a purely rotating field. Thus, in cylindrical coordinates and assuming the machine shaft is along the z-axis, both the r and θ -components need to be considered to accurately characterize the magnetic field at the stator. In addition to the field produced by the rotor, the stator self-field, produced by transport current, and field enhancement due to the back iron need to be included. The magnetic field was determined based on the analysis by Hughes and Miller, presented in [36].

The magnetic field is determined by $\mathbf{B} = \nabla \times \mathbf{A}$ where \mathbf{A} is the magnetic potential, for windings defined by a sine distributed current sheet given by

$$K \sin(p\theta), \text{ where } K = \frac{2T_p h k_w}{\pi r} i \left[\frac{A}{m} \right]. \quad (3.17)$$

T_{ph} is the number of turns per phase, k_w is the winding factor, r is the radius, and i is the current. In two dimensions, the windings are assumed to be infinitely long, thus the magnetic potential is only in the axial or z direction. Solving Laplace's equation gives the solution to the magnetic potential by

$$\frac{\partial^2 A_z}{\partial r^2} + \frac{1}{r} \frac{\partial A_z}{\partial r} - \frac{p^2}{r^2} A_z = 0. \quad (3.18)$$

For an air cored superconducting machine with an iron environmental shield the solution to the magnitude of the magnetic field determined by Hughes and Miller [36] is given by

$$\begin{aligned} \text{for } r_i < r \quad \begin{cases} B_r \\ B_\theta \end{cases} &= \frac{\mu_0 K}{2} \left(\frac{r_i}{r}\right)^{p-1} \left(1 + \eta \lambda_s \left(\frac{r}{r_s}\right)^{2p}\right) \\ \text{for } r < r_i < r_s \quad \begin{cases} B_r \\ B_\theta \end{cases} &= \frac{\mu_0 K}{2} \left(\frac{r}{r_i}\right)^{p+1} \left(1 \pm \eta \lambda_s \left(\frac{r_i}{r_s}\right)^{2p}\right) \end{aligned} \quad (3.19)$$

with $\lambda_s = \frac{\mu_s - 1}{\mu_s + 1}$, a function of the permeability, and $\eta = \frac{1 - \left(\frac{r_s}{r_e}\right)^{2p}}{1 - \lambda_s^2 \left(\frac{r_s}{r_e}\right)^{2p}}$, a function of the iron

geometry, where r_i is the radius of interest and r is the radius of the winding. As depicted in Fig. 3.4, r_s is the inner radius of the back iron while its outer radius is represented by r_e . B_r and B_θ are the r and θ components of the magnetic field, respectively. The permeability of free space is denoted by μ_0 and the iron enhancement factor is given by $\left(1 \pm \eta \lambda_s \left(\frac{r_i}{r_s}\right)^{2p}\right)$.

μ_s is assumed to be very large, resulting in $\lambda_s \sim 1$ and $\eta \sim 1$. The field radius is taken as r_2 and r_0 for the rotor and stator, respectively. The radius of interest is taken to be r_0 . It is clear that for the rotor field, our radius of interest, r_0 , satisfies the second condition in Eqn. (3.19), $r_2 < r_0 < r_s$. However, for the stator field, both the winding radius and the radius of interest are taken as r_0 , which doesn't satisfy either of the conditions in Eqn. (3.19). Setting $r = r_i = r_0$, both conditions result in the same B_r , but discrepancies arise

for B_θ . Currently the field is calculated using the second condition. Applying the above stated assumptions, Eqn. (3.17) simplifies to

$$\text{for } r_2 < r_0 < r_s \quad \begin{cases} B_{Rt_r} \\ B_{Rt_\theta} \end{cases} = \frac{\mu_0 K_r}{2} \left(\frac{r_2}{r_0}\right)^{p+1} \left(1 \pm \left(\frac{r_0}{r_s}\right)^{2p}\right), \quad (3.20)$$

for the magnitude of the magnetic field at r_0 produced by the rotor and

$$\text{for } r_0 < r_0 < r_s \quad \begin{cases} B_{St_r} \\ B_{St_\theta} \end{cases} = \frac{\mu_0 K_s}{2} \left(\frac{r_0}{r_0}\right)^{p+1} \left(1 \pm \left(\frac{r_0}{r_s}\right)^{2p}\right), \quad (3.21)$$

for the magnitude of the magnetic field at r_0 produced by the stator. The electrical loading of the rotor is K_r , while K_s is the stator electrical loading. The peak field in the stator at r_0 is determined by

$$B_{St_{max}} = \left[\left(B_{Rt_r} + B_{St_r} \cos(\varphi) + B_{St_\theta} \sin(\varphi) \right)^2 + \left(B_{Rt_\theta} + B_{St_r} \sin(\varphi) + B_{St_\theta} \cos(\varphi) \right)^2 \right]^{1/2}, \quad (3.22)$$

where $\varphi = \pi/2p$ is the phase angle between the rotor and stator magnetic fields.

3.3.3 AC Loss Corrections

The only change made to the eddy current and coupling losses involved updating the magnetic field from B_0 to $B_{St_{max}}$, accounting for the maximum field in the stator. Lorin et al. developed scaling laws for semi-analytical fit data, based on numerical simulations to determine the hysteresis losses, produced by an elliptical field [13]. This method, summarized below, was implemented to improve the analysis of the hysteresis losses in SIZING.

The variables, J_c, μ_0, r, E_c , the electric field criterion, Q, b_0, f, φ, k , and n , the n -value, describe the losses in a superconducting filament. From these variable, Lorin et al.

derived six dimensionless parameters describing the losses, b^* , f^* , q^* , φ , k , n [13]. The reduced field, b^* , is given by

$$b^* = \frac{b_0\pi}{2J_c\mu_0 r}. \quad (3.23)$$

The reduced frequency, f^* , is

$$f^* = \frac{fJ_c\mu_0\pi r^2}{E_c}. \quad (3.24)$$

The reduced losses, q^* , are defined as

$$q^* = \frac{Q}{\mu_0 J_c^2 r^4}. \quad (3.25)$$

From these a loss function can be defined as $\frac{q^*}{b^{*2}}$, representing the ratio between dissipated and available energy [13].

To determine losses for an elliptical field, φ is initially set to zero, and the losses are scaled for multiple k-values by the functions $\beta_{in}(k)$ and $\beta_{out}(k)$, to ensure a fit over various k-values. A scaling laws fit the loss function, $\frac{q^*}{b^{*2}}$, with the critical state model by defining the parameter c_n , given by Eqn. (3.26), which represents the balance between the magnetic field strength and the penetration depth [13],

$$c_n = \left(\frac{f^*}{b^{*n-1}}\right)^{-\frac{1}{n}} = \left(\frac{b^{*n-1}}{f^*}\right)^{\frac{1}{n}} = \frac{b_0\pi}{2\mu_0 J_c r} \left(\frac{2E_c}{b_0 f \pi^2 r}\right)^{\frac{1}{n}}. \quad (3.26)$$

Then the reduced losses given by,

$$Q^* = \frac{X^*}{\left[0.5(1+X^{*\beta_{in}(k)})\right]^{\beta_{out}(k)}} \quad (3.27)$$

were normalized by the functions $max_{ell}(n, k)$ and $x_{ell}(n, k)$ which determine the maximum value of the losses and location, respectively, for each n-value, such that [13]

$$Q^* = \frac{1}{max_{ell}(n, k)} \left(\frac{q^*}{b^{*2}}\right) \text{ and} \quad (3.28)$$

$$X^* = \frac{c_n}{x_{ell}(n,k)}. \quad (3.29)$$

The losses for $\varphi = 0$ are determined by solving for Q in Eqn. (3.25) where q^* is calculated from (3.28) and Q^* from (3.27). For different phase angles, $\varphi \neq 0$, the losses can be determined by [13]

$$\frac{Q(c_n, k, n, \varphi)}{Q(c_n, k, n, \varphi=0)} = \frac{1-\gamma}{2} (1 + \cos \varphi) + \gamma, \quad (3.30)$$

where $\gamma = \frac{Q(c_n, k, n, \varphi=\pi)}{Q(c_n, k, n, \varphi=0)}$, is the ratio between the losses with a phase angle of π and 0.

The general solution for magnetization losses in a superconducting stator under the influence of an elliptical field is given by [13]

$$Q_M \left(c_n, k, n, \varphi = \frac{\pi}{2p} \right) = Q(c_n, k, n, \varphi = 0) \left[\frac{1-\gamma}{2} (1 + \cos \varphi) + \gamma \right] \\ * f \left(\frac{1}{\pi r^2} \right) \left(\frac{1}{1+M_{Cu-SC}} \right) \left(1 + \left(\frac{J_{ST}}{J_c} \right)^2 \right) V_{St}. \quad (3.31)$$

In SIZING, the value for k was taken as the average value determined in AMBER. AMBER calculates and records the ellipticity, k , in each wire of one stator phase. Averaging this value over one phase gives k_{avg} , the approximate field ellipticity for a given simulation. k_{avg} was recorded for multiple simulations with the power varying from 13000 kW to 6000 kW and the speed varying from 8000 rpm to 3000 rpm. For each case, k_{avg} is plotted against torque in Fig. 3.12 and against the rotor-stator air gap in Fig. 3.13. There is no clear correlation between k and the rotor-stator air gap and possibly a slight negative correlation against torque. k_{avg} ranged from 0.24 to 0.38 with a mean of 0.32. Since the range is small and there is no clear correlation, SIZING assumes the average value of $k = 0.32$.

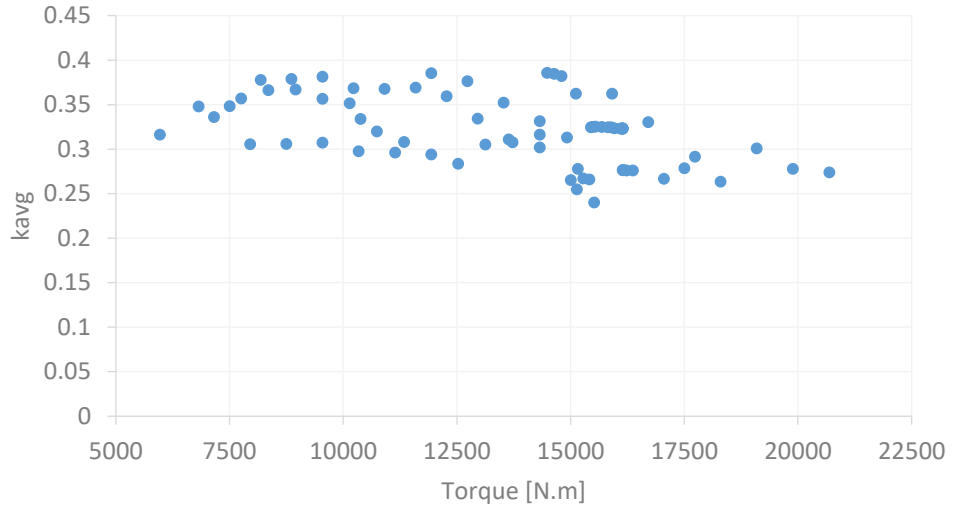


Figure 3.12: Field ellipticity plotted against machine torque

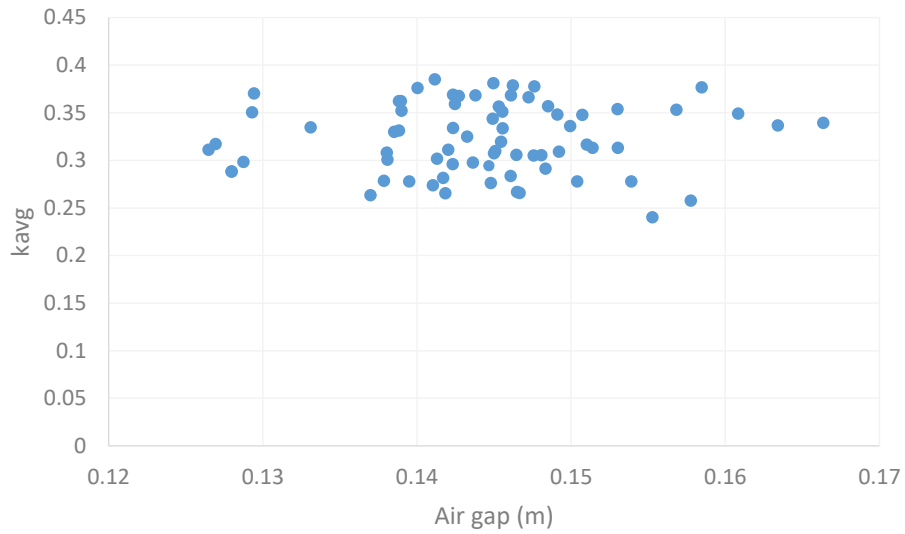


Figure 3.13: Field ellipticity plotted against the rotor-stator air gap

To ensure that this assumption did not affect the results, the average value of k was recorded for each simulation to see if assuming a value of 0.32 for the ellipticity had any significant effect on the final results. Fig. 3.14 plots k_{avg} against torque after updating the program, showing no clear correlation. The average value remained at 0.32 with the maximum increasing to 0.4.

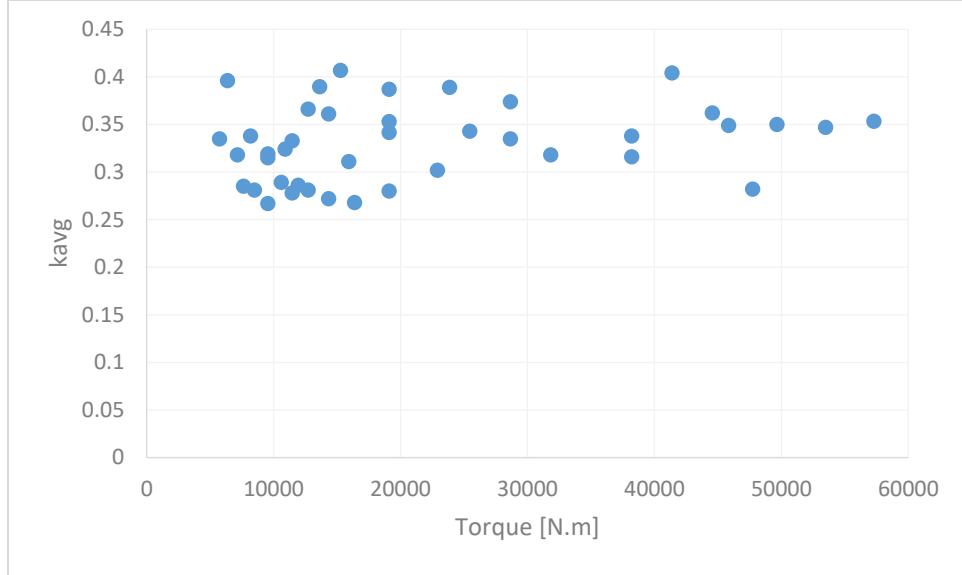


Figure 3.14: Field ellipticity plotted against machine torque for the updated model

Additional simulations were conducted for several cases, outlined in Table 3.1, where the difference in k_{avg} returned by AMBER was greater than 0.32 ± 0.05 . These cases were run again, but with k changed from 0.32 to k_{avg} (detailed in the last column of Table 3.1) in SIZING for each case. Adjusting the ellipticity slightly improved the hysteresis losses. The difference in results, plotted in Figure 3.15, changed the error by a maximum of 3 percentage points. Therefore assuming $k = 0.32$ did not have a significant impact on the loss solutions.

Table 3.1: Simulations with Significant Ellipticity Differences

| Case Number | Power [kW] | Speed [rpm] | k (SIZING) | k_{avg} (AMBER) |
|-------------|------------|-------------|--------------|-------------------|
| 1 | 10000 | 7000 | 0.32 | 0.39 |
| 2 | 10000 | 4000 | 0.32 | 0.39 |
| 3 | 8000 | 5000 | 0.32 | 0.407 |
| 4 | 6000 | 9000 | 0.32 | 0.396 |
| 5 | 6000 | 3000 | 0.32 | 0.39 |

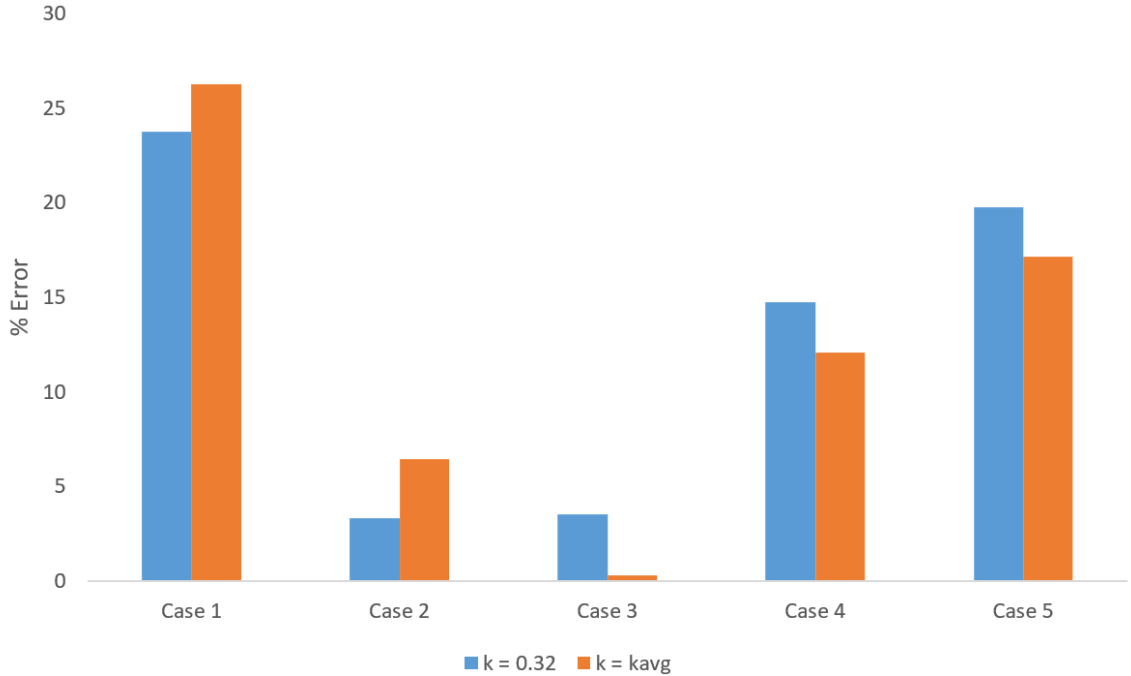


Figure 3.15: Effect of ellipticity on hysteresis losses

3.3.4 Copper Stator

Most superconducting motors and generators do not use superconducting windings for the stator because the alternating fields induce large losses, counteracting the benefits of using superconductor technology. Due to low power densities, conventional machines must be massive in order to produce the same amount of power as superconducting machines. If AC losses can be limited to 0.1% of the total power output, then a fully superconducting machine is likely to be lighter than those incorporating a copper stator [5], [28].

To test this theory, material properties for copper were added to the materials file used in SIZING allowing the user to define the stator as either normal or superconducting. In the case of a copper stator, AC losses become irrelevant and resistive losses dominate, calculated by

$$Q_{Cu} = J^2 \rho_{Cu} V_{St}. \quad (3.32)$$

J is user defined current density in the stator, set to 5 and 7 A/mm^2 in these simulations. The resistivity of copper, ρ_{Cu} , is temperature dependent. Taking this into account a linear regression has been implemented to determine $\rho_{Cu}(T_{op})$ based on NIST data compiled by R. A. Matula [37]. Using SIZING, the simulations were performed comparing the mass between superconducting machines with a Cu and MgB_2 stator.

3.3.5 SIZING as a Stand-Alone Program

Originally, SIZING was not a program, but a function in AMBER. The goal was to separate SIZING, changing it from a function dependent on AMBER into a standalone program. While AMBER produces results based on time consuming numerical solutions, SIZING relies on analytical equations. The greatest advantage of separating SIZING is reduced computation time. On a typical laptop SIZING solves simulations in minutes compared to the hours required by AMBER. Separating SIZING along with increasing its fidelity will provide users with quick estimates for superconducting machine geometry, mass, and losses.

3.4 AMBER Updates

The magnetic field used in eddy current and coupling calculations was significantly less than the actual field in the stator, thus underestimating the losses. Changing the magnetic field in AMBER allows the eddy current and coupling losses to be calculated using the peak field in the conductor. Now the solutions to hysteresis, eddy current, and coupling losses all consider the same magnetic field.

4. RESULTS

In order to gauge how much the accuracy of SIZING improved, 36 different cases were simulated with the user defined power and speed for each case outlined in Table 4.1 and compared to the results from the original model.

Table 4.1: Simulation power and speed specifications

| Speed [rpm] | 2000 | 3000 | 4000 | 5000 | 6000 | 7000 | 8000 | 9000 | 1000 |
|-------------|-------|-------|-------|-------|-------|-------|-------|-------|-------|
| Power [kW] | 12000 | 12000 | 12000 | 12000 | 12000 | 12000 | 12000 | 12000 | 12000 |
| | 10000 | 10000 | 10000 | 10000 | 10000 | 10000 | 10000 | 10000 | 10000 |
| | 8000 | 8000 | 8000 | 8000 | 8000 | 8000 | 8000 | 8000 | 8000 |
| | 6000 | 6000 | 6000 | 6000 | 6000 | 6000 | 6000 | 6000 | 6000 |

4.1 Magnetic Field

Including both the alternating and rotating parts of the magnetic field (r- and θ -components), along with the stator self-field in the magnetic field solution considerably reduced the percent error between the analytical (SIZING) and the actual (AMBER) magnetic field in the stator. Fig. 4.1 compares the percent error from the updated model, shown in orange, to that of the original model, shown in blue. The average error for the updated model was 11.5%, which is a reduction of almost 50 percentage points from the original model which had an average error of 64%.

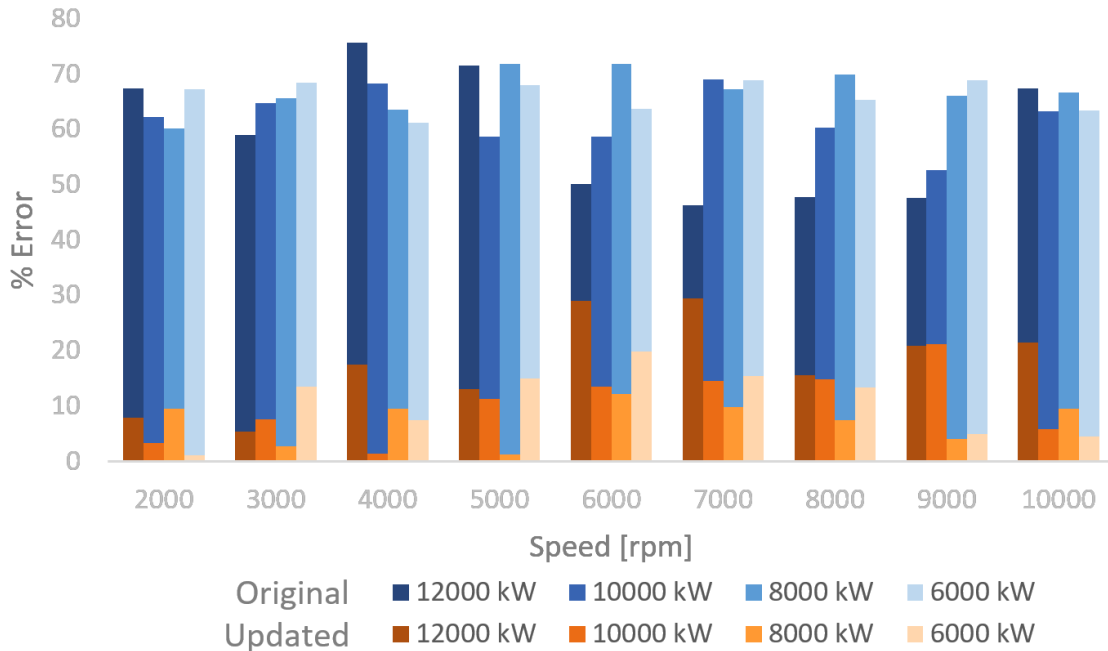


Figure 4.1: Comparison of the percent error for the magnetic field between SIZING and AMBER in the original (blue) and updated (orange) program

4.2 AC Losses

The magnitude of the magnetic field is an integral parameter in loss calculations. Thus improving the accuracy of magnetic field lead to improvements in the AC losses. The overall average percent error for the total AC losses dropped significantly from 157% in the original model to 22% in the updated model. A maximum error of 70.6% occurred for 6000 kW-8000 rpm case, while a minimum error of 0.85% occurred for the 6000 kW-3000 rpm case. Fig. 4.2 compares the percent error for the total AC losses for each simulation between the original and the updated models. In total, 19 of the 36 simulations had a percent error below 20%, 14 with error below 10%, and 6 had less than 5% error. These are significant improvements when compared to the original model which had a minimum error of 52% and only 6 simulations were below 100% error.

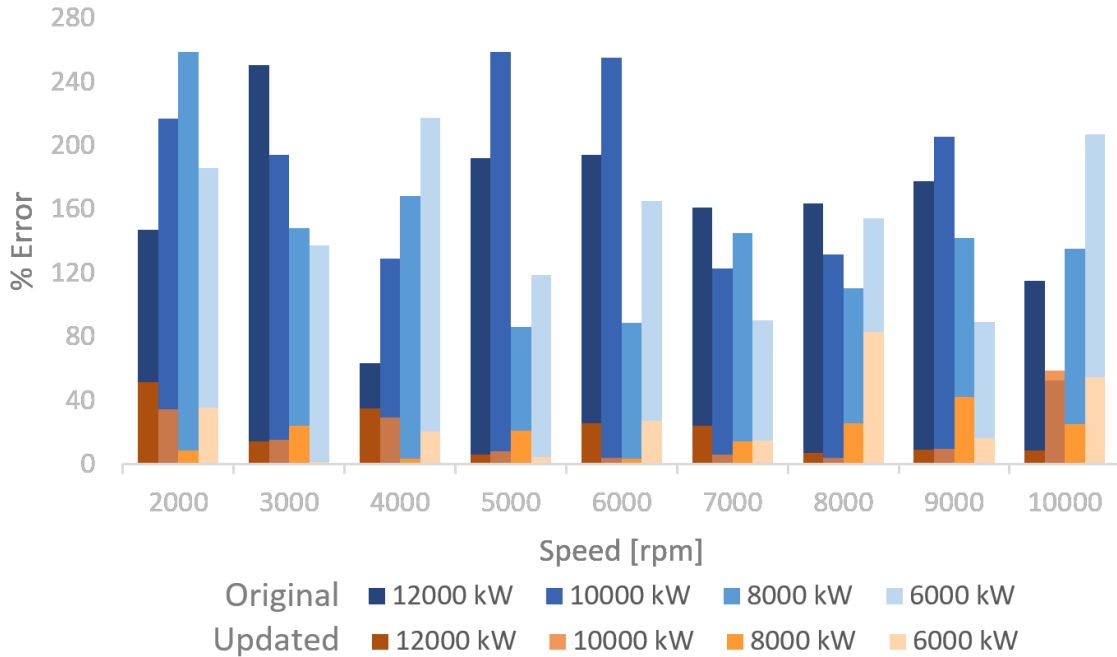


Figure 4.2: Comparison of the percent error for the total losses between SIZING and AMBER in the original (blue) and updated (orange) program

The optimization in SIZING is still constrained by the maximum allowable AC losses, which is set to 10500 W. In most cases, the best solution was found when the AC losses were at their maximum value. However, for several cases: 8000kW-8000 rpm, 6000 kW-8000 rpm, 8000kW-2000 rpm, and 6000kW-2000 rpm, SIZING was able to find a solution without maximizing the losses. Fig. 4.3 shows the difference between the AC losses calculated in SIZING and then refined by AMBER. In most case the losses determined by AMBER are smaller than those produced by SIZING, but in a handful of simulations, specifically when $P = 12000 \text{ kW}$, AMBER produced larger losses.

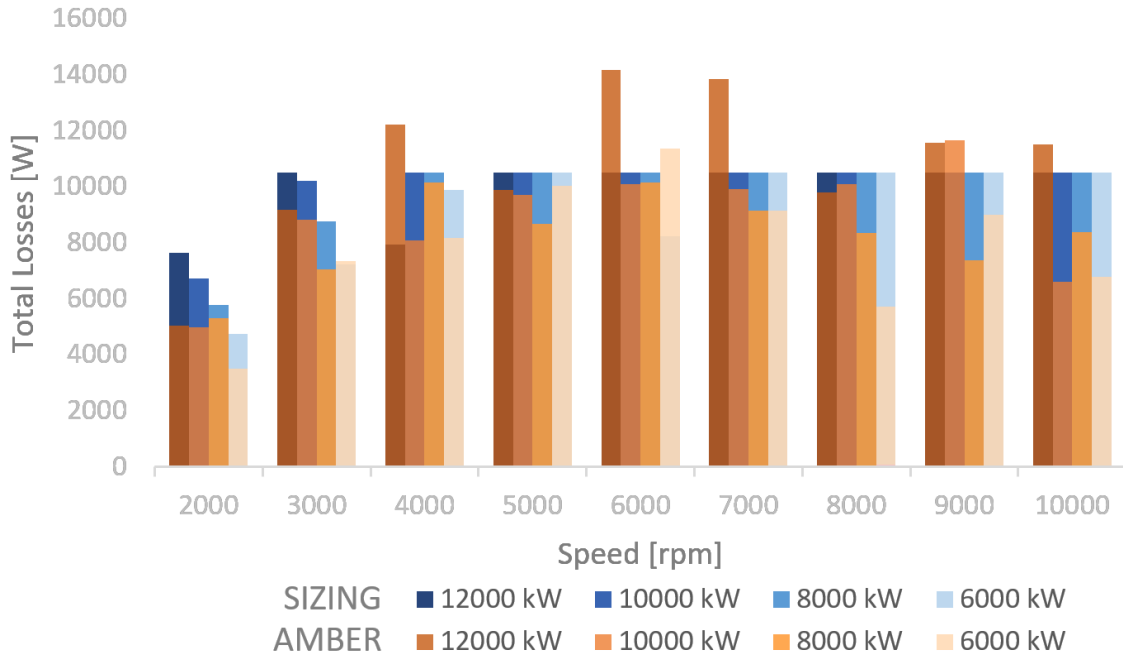


Figure 4.3: Comparison of total AC losses between SIZING (blue) and AMBER (orange) in the updated model

Not only did the error, between SIZING and AMBER, decrease, but the loss distribution also changed, shown in Figs. 4.4 and 4.5 for cases with $P = 8000 \text{ kW}$. Previously, SIZING produced results, depicted in blue in Fig. 4.4, where the hysteresis losses clearly dominated. However, AMBER calculated significantly reduced hysteresis losses that barely dominated. Now coupling losses dominate and, as can be seen in Fig. 4.5 and the losses calculated in SIZING closely reflect those from AMBER.

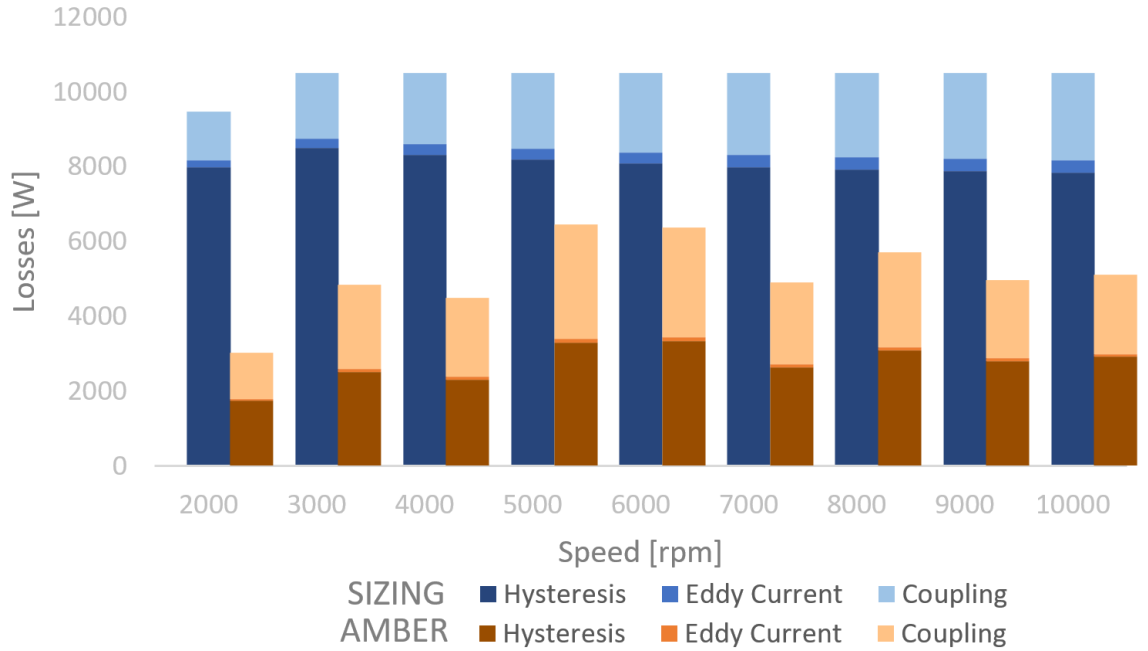


Figure 4.4: AC Loss distribution from the original model for SIZING (blue) and AMBER (orange). Only cases for $P = 8000 \text{ kW}$ are shown.

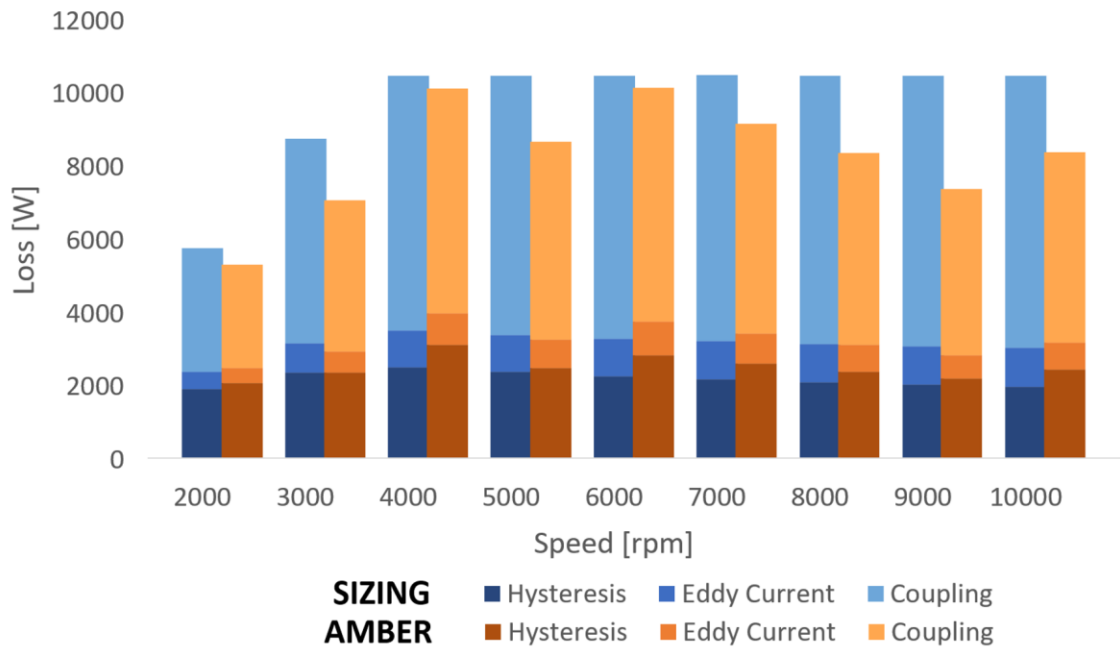


Figure 4.5: AC Loss distribution from the updated model for SIZING (blue) and AMBER (orange). Only cases for $P = 8000 \text{ kW}$ are shown.

4.2.1 Hysteresis Losses

The improvements to analysis of the hysteresis losses decreased the percent error, between SIZING and AMBER, from an average of 264% in the original to 18.5% in the new model, depicted in Fig. 4.7. Now 25 out of 36 simulations are below 20% error with 10 below 10% error, whereas not a single solution from the original model was below 100% error.

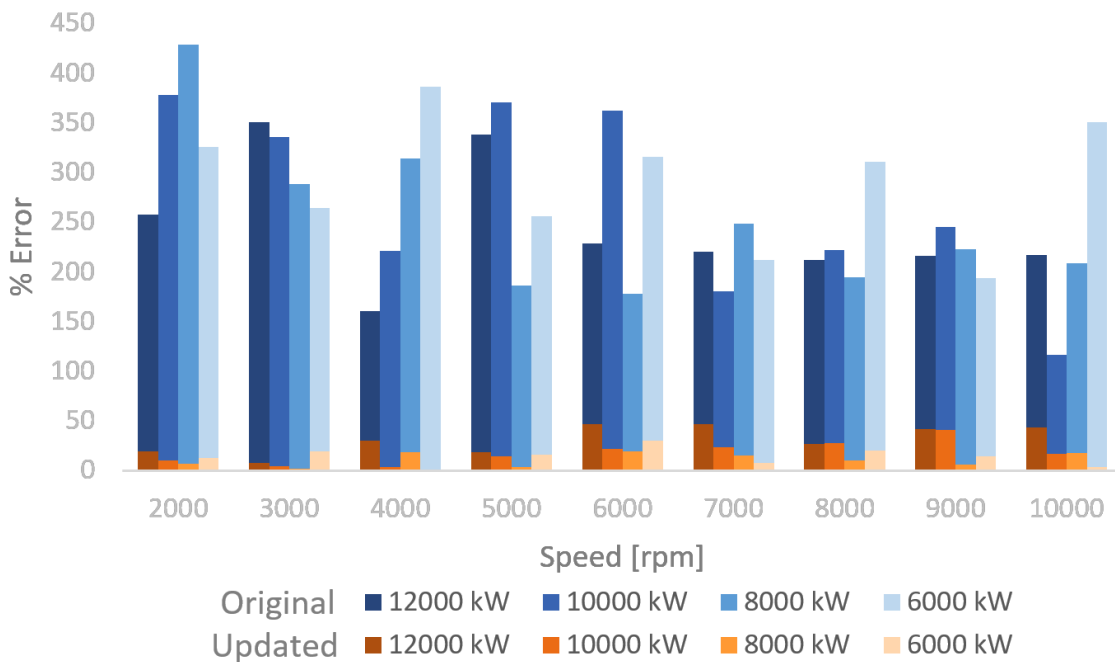


Figure 4.7: Comparison of the percent error for the hysteresis losses between SIZING and AMBER in the original (blue) and updated (orange) program

4.2.2 Eddy Current Losses

The average percent error for the eddy current losses dropped from 350% in the original model to 31% in the new model. Fig. 4.8 compares the percent error between the two models. The maximum error was 111% with a minimum of 1%, where 17 of the 36 cases had less than 20% error.

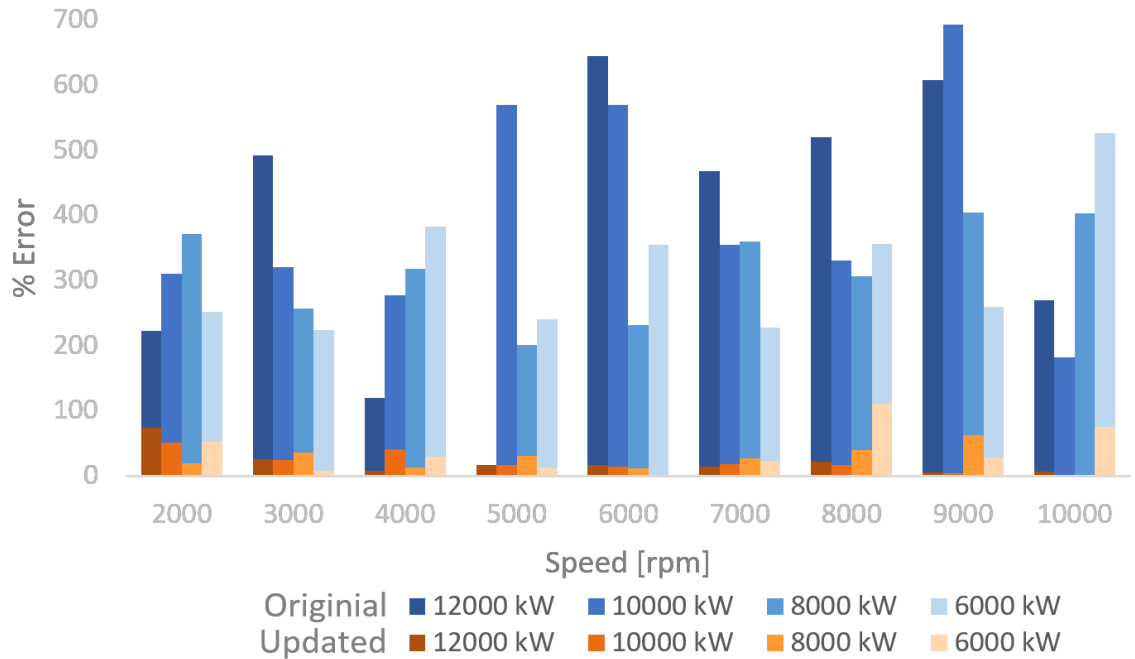


Figure 4.8: Comparison of the percent error for the eddy current losses between SIZING and AMBER in the original (blue) and updated (orange) program

4.2.3 Coupling Losses

Coupling losses saw no improvement, Fig. 4.9, in fact they got slightly worse. The average error increased from 27% to 30% and the maximum error increased from 100% to 111%.

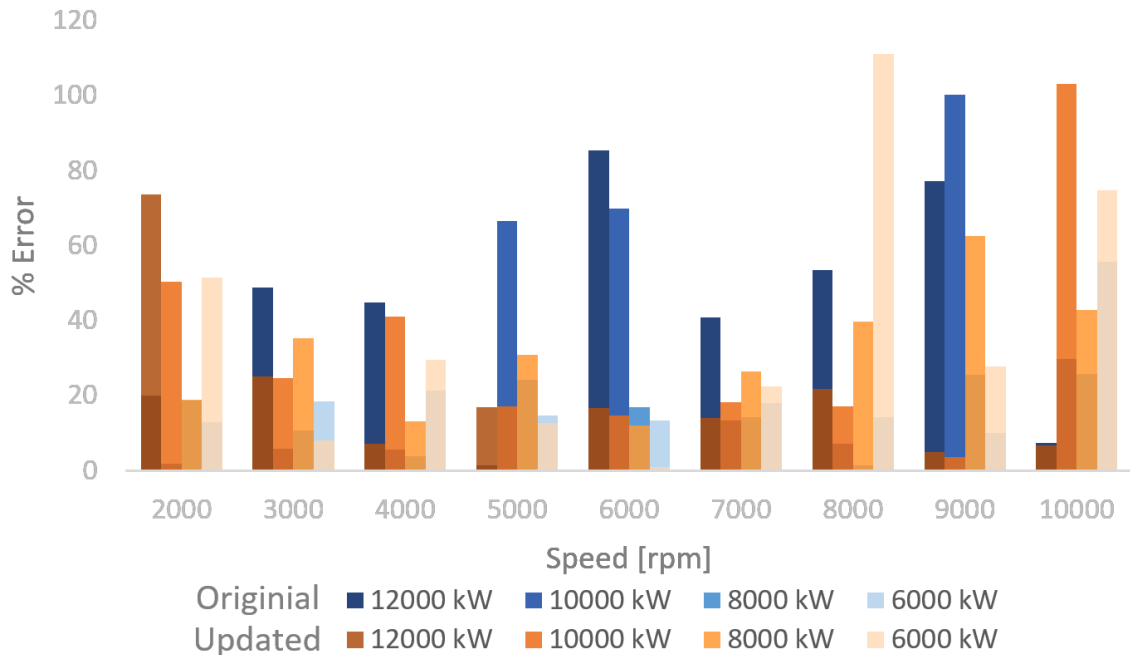


Figure 4.9: Comparison of the percent error for the coupling losses between SIZING and AMBER in the original (blue) and updated (orange) program

4.3 Mass

All these improvements resulted in better estimations of machine size. Fig. 4.10 shows how much the percent error dropped for each simulation. Fig. 4.11 compares the difference in the active mass determined SIZING and AMBER in the updated version, which is significantly less than the original model, Fig. 4.12. Not only is the difference between low and high fidelity models significantly reduced, but the active mass has also decreased. Comparing Figs. 4.11 and 4.12, it is clear that, in the original SIZING, the overestimation of the losses prevented the determination of the best solution. Therefore, the low fidelity results from SIZING were impeding AMBER’s ability to produce the best solution.

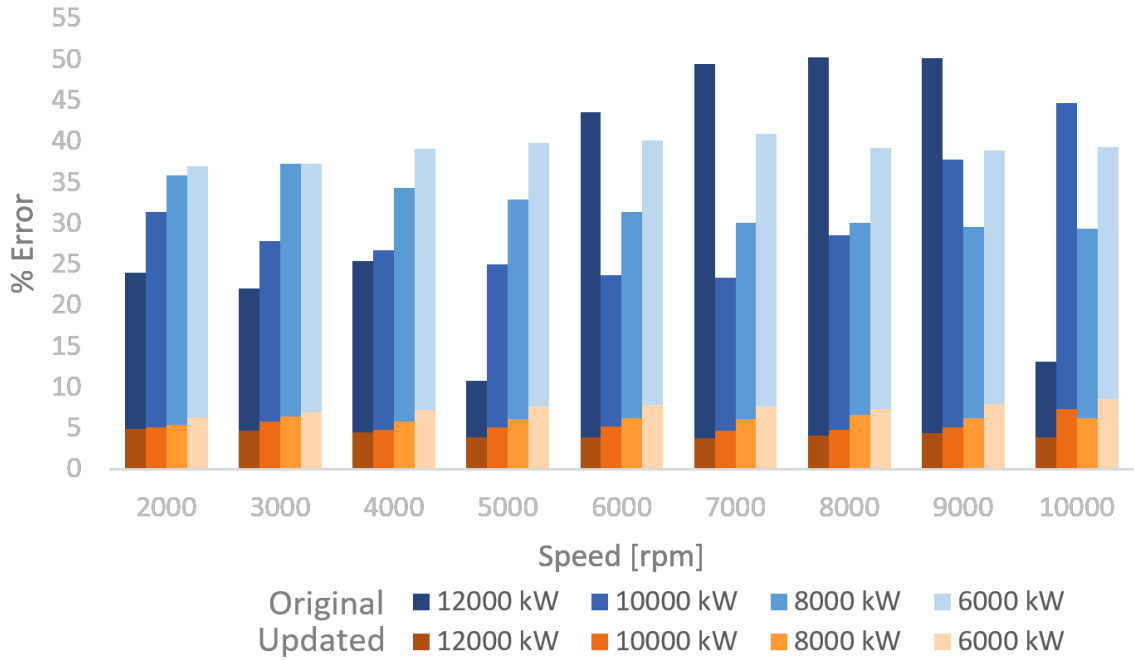


Figure 4.10: Comparison of the percent error for the mass between SIZING and AMBER in the original (blue) and updated (orange) program

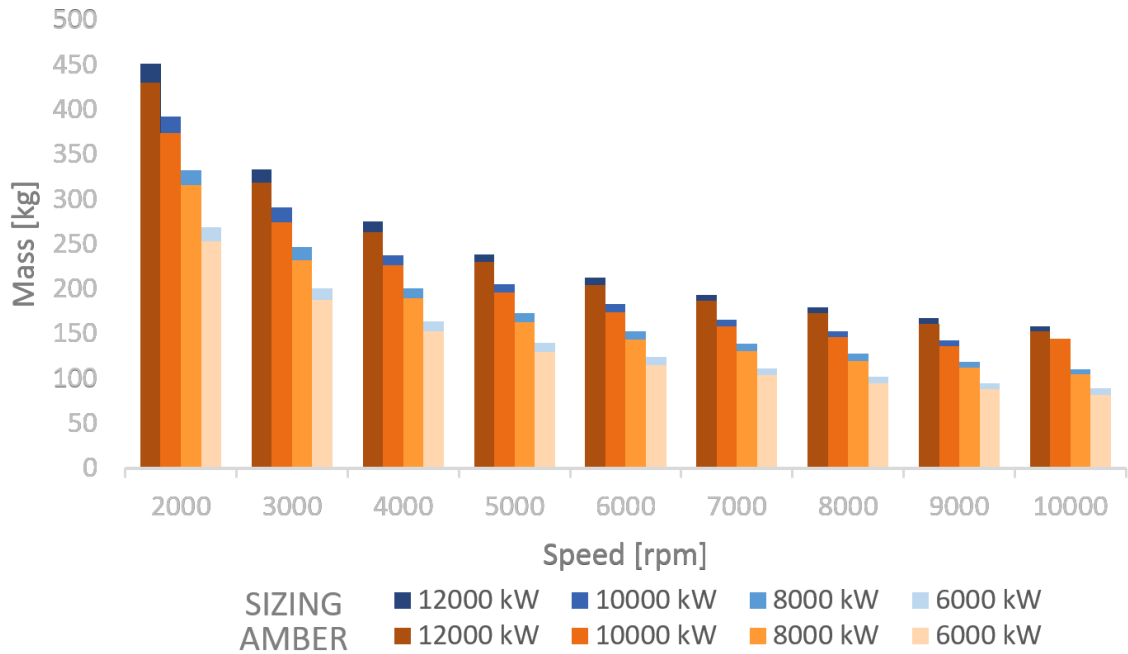


Figure 4.11: Difference in mass between SIZING (blue) and AMBER (orange) for the updated program

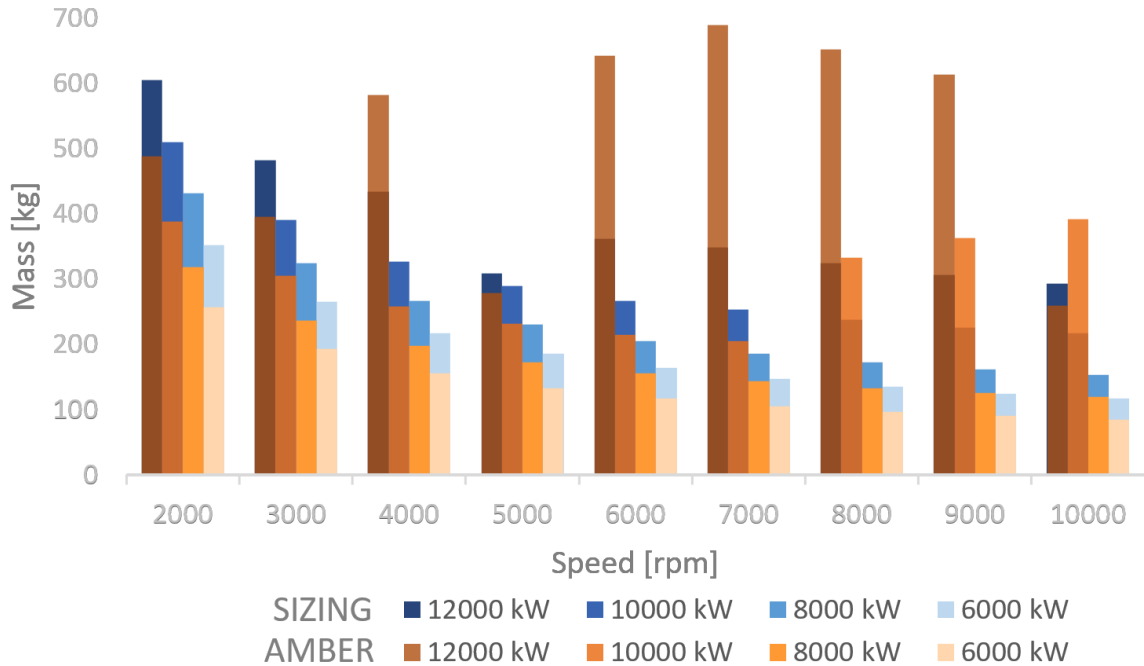


Figure 4.12: Difference in mass between Sizing (blue) and Amber (orange) for the original program

4.4 Copper v. MgB₂ Stator

The results presented in this section were produced by SIZING, simulations in AMBER were not considered. The 36 scenarios, detailed in Table 4.1, were run for a superconducting machine with the stator material defined as MgB₂ as well as Cu. When the current density in the copper stator is set to 5 A/mm^2 , the resulting active mass is larger than that of a fully superconducting machine, Fig. 4.13.

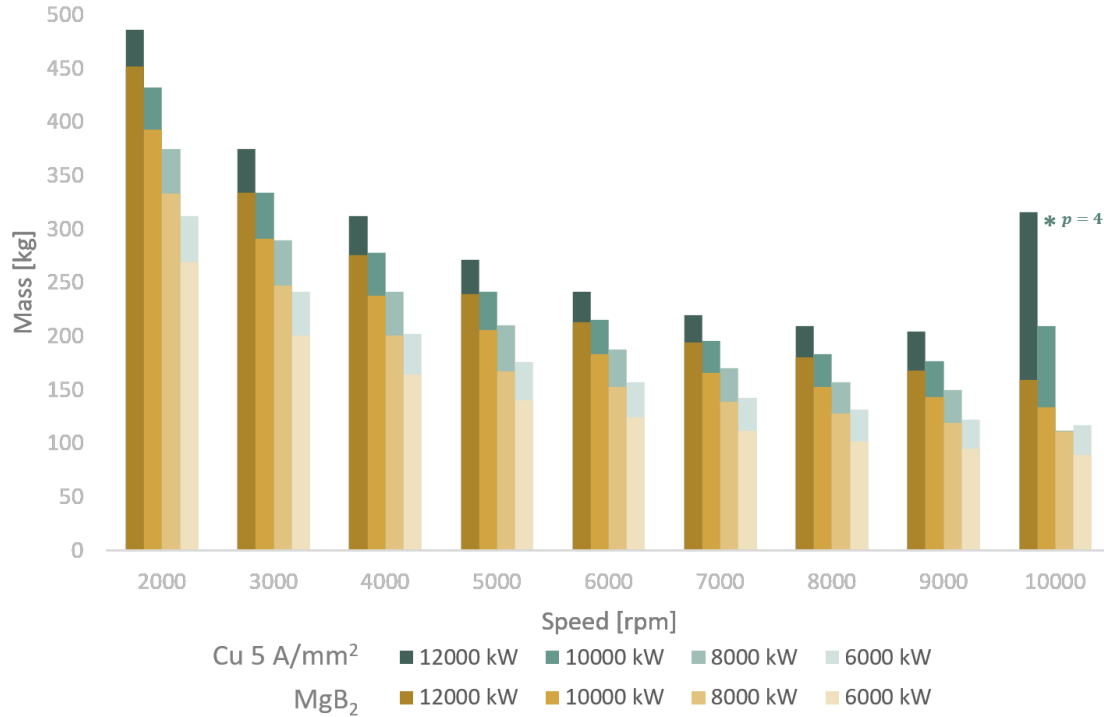


Figure 4.13: Active machine mass for a superconducting machine with a copper stator (orange) with $J = 5 \text{ A/mm}^2$ and an MgB₂ stator (blue)

*At 12000 kW and 10000 rpm, a solution could not be found above four pairs of poles, which is why that case is much more massive than other cases, which contain five pairs of poles.

Increasing the current density to 7 A/mm^2 in the copper stator produces varied results, Fig. 4.14. At higher powers and lower speeds, a copper stator produces a less massive machine. The largest difference occurs at 12000 kW and 2000 rpm where the fully superconducting machine is 54 kg heavier than the partially superconducting machine. However, as the speed increases, this difference decreases, and in some cases, the fully superconducting machine is lighter. At lower powers, 8000 kW and 6000 kW, and above 5000 rpm the copper stator is more massive, though in most cases it only weighs 1-2 kg more than an MgB₂ stator. Thus using an MgB₂ stator won't necessarily weigh less than a copper stator, even though superconductors have much higher power densities than copper. Whether or not an MgB₂ stator would be advantageous in reducing mass depends the power and speed requirements along with the operating current in the copper.

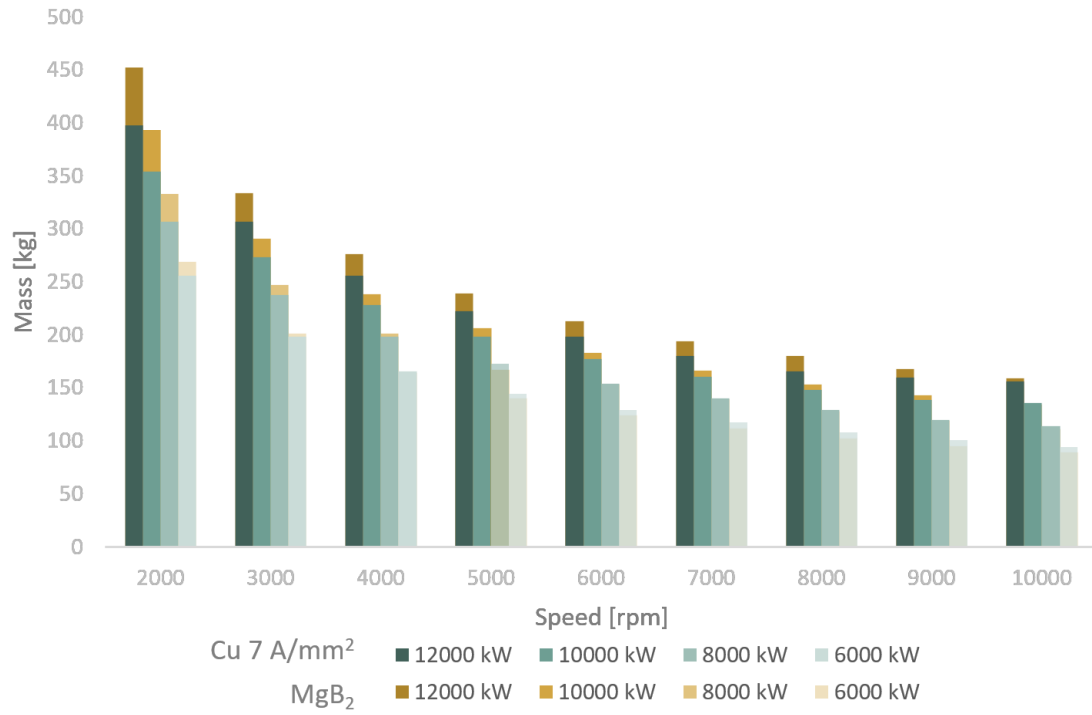


Figure 4.14: Active machine mass for a superconducting machine with a copper stator (orange) with $J = 7 \text{ A/mm}^2$ and an MgB₂ stator (blue)

5. CONCLUSIONS

When considering turboelectric generators and motors as an alternative for aircraft propulsion, the main concern is the weight of the system [7], [12]. Additionally, in order for the system to be feasible, the efficiency must be high, which can be controlled in the design process by limiting the maximum AC losses. This constraint, in turn, affects the machine mass as described in section 3.2. Therefore, calculations of machine mass depend on accurate AC loss solutions.

The magnitude and orientation of the magnetic field strongly influence the AC losses. Implementing calculations for an elliptical field improved solutions for hysteresis and eddy current losses. However, coupling losses experienced little improvement and should be investigated further to find better solutions. These corrections significantly reduced the percent error, between SIZING and AMBER, of the total AC losses, producing smaller machines. However, there are still some reasonably large discrepancies between the two models, up to 84% in some cases. While this is greatly reduced from the 260% maximum error produced by the original program, future work should investigate why some simulations produce larger errors and how to maintain consistently low error across all cases. Even though SIZING still has some discrepancies, the errors have been significantly reduced and it can now be used on its own, without relying on AMBER. This allows the user to run fast simulations to get an estimate for a machine's size, weight, and losses and construct preliminary models.

Possible sources of error could be attributed to assumptions made about the magnetic field and its ellipticity. At the stator average radius, r_0 , $B_{ST\theta}$ was assumed to satisfy the second condition of Eqn. (3.19). However, in this situation there is no solution

for B_θ , that is when the radius of the field winding is equivalent to the radius of interest. Developing an equation for $r = r_i$ will likely increase the accuracy of the magnetic field solution from the stator at r_0 , leading to higher fidelity loss solutions. In SIZING, the field ellipticity, k , was approximated as k_{avg} calculated in AMBER. While this proved to be a good estimation, implementing an analytical equation for k may decrease hysteresis loss errors.

Assuming free cooling, that is, using LH2 to cool the machines before it is used as a fuel source for the generators [7], [12], the efficiency, calculated by $\eta = \frac{P-Q_{tot}}{P}$, is 99.9% for a fully superconducting machine, which corresponds to the data presented by NASA in [12], where the AC losses account for approximately 0.1% of the total machine power. Since AC losses are low, fully superconducting machines could be a viable alternative to partially superconducting machines which use copper stators. Whether or not using MgB₂ stators produces lighter machines depends on the current density in Cu stator. Employing a higher current density reduces the amount of conductor needed to produce the required power, resulting in lighter machines. However, lower current densities result in active masses heavier, than those of fully superconducting machines, incorporating an MgB₂ stator.

REFERENCES

- [1] "FAA Aerospace Forecast Fiscal Years 2016-2036," 2017. [Online]. Available: https://www.faa.gov/data_research/aviation/aerospace_forecasts/media/FY2016-36_FAA_Aerospace_Forecast.pdf.
- [2] C. Mora , A. G. Frazier, R. J. Longman, R. S. Dacks, M. M. Walton, E. J. Tong, J. J. Sanchez, L. R. Kaiser, Y. O. Stender, J. M. Anderson, C. M. Ambrosino, I. Fernandez-Silva, L. M. Giuseffi, T. W. Giambelluca, "The projected timing of climate departure from recent variability." *Nature*, vol. 502, pp. 183-187, October 2013.
- [3] "Sources of Greenhouse Gas Emissions," 2015. [Online]. Available: <https://www.epa.gov/ghgemissions/sources-greenhouse-gas-emissions>.
- [4] "U.S. Aviation Greenhouse Gas Emissions Reduction Plan," 2015. [Online]. Available: https://www.faa.gov/about/office_org/headquarters_offices/apl/environ_policy_guidance/policy/media/2015_US_Action_Plan_FINAL.pdf
- [5] H. D. Kim, G. V. Brown, J. L. Felder, "Distributed turboelectric propulsion for hybrid wing body aircraft," *Proc. 9th Int. Power. Lift Conf.*, Jul. 2008.
- [6] A. S. Gohardini, G. Doulgeris, R. Singh, "Challenges of future aircraft propulsion: A review of distributed propulsion technology and its potential application for the all electric commercial aircraft," *Progress in Aerospace Sciences*, vol. 47, no. 5, pp. 369-391, July 2011.
- [7] P. J. Masson, G. V. Brown, D. S. Soban, C. A. Luongo, "HTS machines as enabling technology for all-electric airborne vehicles," *Supercond. Sci. Technol.*, vol. 20, no. 8, pp. 748-756, Aug. 2007.

- [8] W. J. Carr, Jr., *AC Loss and Macroscopic Theory of Superconductors*, 2nd ed. New York, NY: Taylor & Francis Inc. 2001.
- [9] P. J. Masson, K. Ratelle, P. A. Delobel, A. Lipardi, C. Lorin, "Development of a 3D sizing model for all-superconducting machines for turbo-electric aircraft propulsion," *IEEE Trans. Appl. Supercond.*, 2013.
- [10] P. J. Masson, P. Tixador, J. C. Ordoez, A. Morega, C. A. Luongo, "Electro-thermal sizing model for HTS motor design," *IEEE Trans. Appl. Supercond.*, vol. 17, no. 2, pp. 1529-1532, Jun. 2007.
- [11] P. J. Masson, D. S. Soban, E. Upton, J. E. Pienkos, C. A. Luongo, "HTS motors in aircraft propulsion: Design considerations," *IEEE Trans. Appl. Supercond.*, vol. 15, no. 2, pp. 2218-2221, Jun. 2005.
- [12] C. A. Luongo, P. J. Masson, T. Nam, D. Mavris, M. Waters, D. Hall, H. D. Kim, G. V. Brown, "Next generation aircraft: A potential new application for high temperature superconductors," *IEEE Trans. Appl. Supercond.*, vol. 19, no. 3, pp. 1055-1068, Jun. 2009.
- [13] C. Lorin, D. Netter, P. J. Masson, "Scaling Law for Hysteresis Losses in Round Superconductors Magnetized by Alternating Rotating or Elliptical Magnetic Fields," *Applied Superconductivity IEEE Transactions on*, vol. 25, pp. 1-12, 2015, ISSN 1051-8223
- [14] "Aircraft Noise Issues," 2016. [Online]. Available: https://www.faa.gov/about/office_org/headquarters_offices/apl/noise_emissions/airport_aircraft_noise_issues/.

- [15] H. D. Kim, J. J. Berton, S.M. Jones, "Low Noise Cruise Efficient Short Take-Off and Landing Transport Vehicle Study," *6th Aviation Technology, Integration and Operations Conf.*, Sept. 2006.
- [16] A. Ko, J. A. Schetz, W. H. Mason, "Assessment of the Potential Advantages of Distributed-Propulsion for Aircraft," ISABE-2003-1094.
- [17] H. D. Kim and J. D. Saunders, "Embedded Wing Propulsion Conceptual Study," *Vehicle Propulsion Integration Symp.*, Oct. 2003.
- [18] E. de la Rosa Blanco, C. A. Hall, D. Crichton, "Challenges in Silent Aircraft Engine Design," AIAA Aerospace Sciences Meeting and Exhibit, Jan 2011. AIAA 2007-454
- [19] J. I. Hilleman, Z. S. Spakovsky, M. Drela, M. A. Sargeant, "Airframe Design for 'Silent Aircraft,'" *AIAA Aerospace Sciences Meeting and Exhibit*, Jan 2011. AIAA 2007-453
- [20] R. H. Thomas, C. L. Burley, E. D. Olson, "Hybrid Wing Body Aircraft System Noise Assessment with Propulsion Airframe Aeroacoustic Experiments," AIAA 2010-3913.
- [21] J. R. Stone and E. A. Krejsa, "Initial Noise Assessment of an Embedded-Wing-Propulsion Concept Vehicle," Apr. 2008.
- [22] J. L. Felder, G. V. Brown, H. D. Kim, J. Chu, "Turboelectric Distributed Propulsion in a Hybrid Wing Body Aircraft," ISABE-2011-1340.
- [23] P. J. Masson, D. S. Soban, E. Upton, J. E. Pienkos, C. A. Luongo, "HTS motors in aircraft propulsion: design considerations," *IEEE Trans. Appl. Supercond.*, vol. 15, no. 2, pp. 2218-2221, 2005.
- [24] P. J. Masson, T. Nam, T. P. Choi, P. Tixador, M. Waters, D. Hall, C. A. Luongo, D. N. Mavris, "Superconducting ducted fan design for reduced emissions aeropropulsion," *IEEE Trans. Appl. Supercond.*, vol. 19, no. 3, pp. 1662-1668, Jun. 2009.

- [25] J. L. Felder, G. V. Brown, H. D. Kim, J. Chu, "Turboelectric distributed propulsion in a hybrid wing body aircraft," Proc. Int. Symp. Air Breath. Engines Conf., pp. 1-20, 2011.
- [26] M. N. Wilson, *Superconducting Magnets*, New York, NY: Oxford Univ. Press, 1983.
- [27] V. L. Ginzburg and E. A. Andryushin, *Superconductivity*, Rev. ed. Hackensack, NJ: World Scientific Publishing Co. Pte. Ltd. 2004.
- [28] J. R. Bumby, *Superconducting rotating electrical machines*, Oxford, U.K.: Clarendon Press, 1983.
- [29] AC Rose-Innes and E. H. Rhoderick, *Introduction to Superconductivity*, 2nd ed. Elmsford, NY: Pergamon Press Ltd., 1978.
- [30] "A comparison of superconductor critical currents," 2017. [Online]. Available: <http://fs.magnet.fsu.edu/~lee/plot/plot.htm>. [May 2017].
- [31] N. Horibe, "Hierarchies in Matter," 2015. [Online]. Available: <http://www.utokyo.ac.jp/en/utokyo-research/feature-stories/hierarchies-in-matter.html>. [May 2017].
- [32] J. Nagamatsu, N. Nakagawa, T. Muranaka, Y. Zenitani, J. Akimitsu, Jun, "Superconductivity at 39 K in magnesium diboride," Nature, vol. 410, no. 6824, pp. 63–64, Mar. 2001.
- [33] D. J. Griffiths, *Introduction to Electrodynamics*, 3rd ed. San Francisco, CA: Pearson, 2008.
- [34] "Products, Technologies and Services that Contribute to the Environment." [Online]. Available:http://www.kobelco.co.jp/english/about_kobelco/csr/environment/2010/1183619.html

[35] G.H. Morgan, "Theoretical Behavior of Twisted Multicore superconducting Wire in a Time-Varying Uniform Magnetic Field," *Journal of Applied Physics*, vol. 41, no. 9, pp. 3673-3679, Aug. 1970.

[36] A. Hughes, T. J. E. Miller, "Analysis of fields and inductances of air-cored and iron-cored synchronous machines," *Proc. Inst. Elect. Eng.*, vol. 124, no. 2, pp. 121-126, Feb. 1977.

[37] R. A. Matula, "Electrical Resistivity of Copper, Gold, Palladium, and Silver," *J. Phys. Chem. Ref. Data*, vol. 8, no. 4, pp. 1147-1298(1159-1161), 1979.